

# Forward-modelling Milky Way Cepheids: selection effects and physical priors in the *Gaia*–*HST* calibration

Richard Stiskalek<sup>1</sup><sup>\*</sup>, Adam G. Riess<sup>2,3</sup>, Harry Desmond<sup>4</sup>, Guilhem Lavaux<sup>5</sup>  
and Dan Scolnic<sup>6</sup>

<sup>1</sup>*Astrophysics, University of Oxford, Denys Wilkinson Building, Keble Road, Oxford, OX1 3RH, UK*

<sup>2</sup>*Space Telescope Science Institute, 3700 San Martin Drive, Baltimore, MD 21218, USA*

<sup>3</sup>*Department of Physics and Astronomy, Johns Hopkins University, Baltimore, MD 21218, USA*

<sup>4</sup>*Institute of Cosmology & Gravitation, University of Portsmouth, Dennis Sciama Building, Portsmouth, PO1 3FX, UK*

<sup>5</sup>*CNRS & Sorbonne Université, UMR 7095, Institut d'Astrophysique de Paris, 98 bis boulevard Arago, F-75014 Paris, France*

<sup>6</sup>*Department of Physics, Duke University, Durham, NC 27708, USA*

Accepted XXX. Received YYY; in original form ZZZ

## ABSTRACT

The advent of high-precision *Gaia* parallaxes for Milky Way Cepheids enables percent-level calibration of the local distance ladder and  $H_0$ . We revisit the Milky Way Cepheid calibration from *Gaia* EDR3 parallaxes using a fully forward-modelled Bayesian framework that simultaneously infers the period–luminosity relation, the *Gaia* parallax zero-point offset, and individual stellar distances while explicitly incorporating the disk geometry of the Galaxy through the distance prior and the selection functions specified in two distinct *HST* SH0ES campaigns. We derive an analytic treatment of the detection probability that accounts for magnitude, parallax, period, and extinction cuts and reduces the selection treatment to a tractable integral over distance and sky position. Posterior predictive checks show that this generative model matches well the observed distributions of parallaxes, magnitudes, and periods. Modelling Galactic structure and survey truncation self-consistently in a Bayesian framework yields period–luminosity parameters that agree with the SH0ES maximum-likelihood values at the  $<0.5\sigma$  level, a consequence, we show, of the small intrinsic scatter of the Cepheid period–luminosity relation. Adopting, as recently advocated, a uniform-in-volume prior without simultaneously accounting for selection leads to a  $\sim 0.05$  mag bias in the period–luminosity zero-point and posterior predictive distributions incompatible with the observed data; this shift is mostly driven by the omission of the selection model. A consistent Bayesian treatment of Galactic structure and selection effects reinforces the local distance-ladder determination of  $H_0$ , and hence the Hubble tension with early-Universe inferences.

**Key words:** methods: statistical – stars: variables: Cepheids – stars: distances – distance scale – cosmological parameters

## 1 INTRODUCTION

The  $\sim 5\sigma$  discrepancy between local distance-ladder and cosmic microwave background (CMB)-calibrated inferences of  $H_0$ , known as the Hubble tension, is one of the most pressing problems in cosmology (e.g. Riess et al. 2022a; Planck Collaboration et al. 2020; Louis et al. 2025; Camphuis et al. 2025; Freedman et al. 2025; Di Valentino et al. 2025). While there are many routes to local  $H_0$ , which contribute to the overall tension (see H0DN Collaboration et al. 2025 for their

covariance-weighted combination), the sharpest local constraint comes from the specific combination of *Gaia* EDR3 parallaxes, Cepheids, and Type Ia supernovae. This motivates a careful examination of the statistical assumptions entering the Milky Way (MW) Cepheid calibration.

In this work, we prise open the MW calibration and model it star-by-star. We construct the first Bayesian forward model of the MW Cepheid population that explicitly accounts for the sample selection function, incorporates the thin-disk geometry of the Galaxy as a distance prior, and infers the intrinsic population properties jointly with the period–luminosity relation and the *Gaia* parallax zero-point

\* richard.stiskalek@physics.ox.ac.uk

offset. In particular, we show that the reduced Hubble tension reported by Högas & Mörtzell (2026, hereafter HM26), who adopted a uniform-in-volume distance prior without selection modelling, is an artefact of that omission. We show that when Galactic disk geometry and survey truncation are modelled consistently, the inferred period–luminosity parameters agree well with the maximum-likelihood values obtained by SH0ES from their parallax-space regression — a consequence, we show, of the small intrinsic scatter of the Cepheid period–luminosity relation. Adopting a uniform-in-volume prior without selection modelling induces a bias. The prior describes the characteristics of the underlying population while the selection function determines which of those objects enter the sample; ignoring the latter while specifying the former generates mock populations inconsistent with the observed sample.

The Cepheid distance scale has been extensively tested against potential astrophysical systematics. JWST observations have ruled out unrecognised photometric crowding in extragalactic hosts as a significant contributor to the tension, with analyses of more than 1000 Cepheids in N4258 and up to 19 SN Ia hosts finding no evidence for bias in Hubble Space Telescope (*HST*) photometry (Riess et al. 2024, 2025). A second key uncertainty for the parallax-based Cepheid calibration is the *Gaia* parallax zero-point offset,  $\delta_{\varpi}$ . While the EDR3 calibration models  $\delta_{\varpi}$  as a function of magnitude, colour, and ecliptic latitude (Lindgren et al. 2021), it remains weakly constrained for bright stars like MW Cepheids ( $G < 9$  mag), a brightness range where EDR3 lacks calibration sources. The SH0ES analysis (Riess et al. 2021, hereafter R21) combined high- and low-parallax samples of Cepheids with *HST* photometry to jointly measure the offset (which is additive) and the Cepheid luminosity (which is multiplicative), yielding  $\delta_{\varpi} = -14 \pm 6 \mu\text{as}$ . Independent validations using asteroseismology, photometric parallaxes, red clump stars, eclipsing binaries, and orbital parallaxes generally favour residual offsets between 0 and  $-20 \mu\text{as}$ , implying that the official correction overestimates the zero-point for bright stars by  $\sim 15 \mu\text{as}$  (Zinn 2021; Groenewegen 2021; Huang et al. 2021; Fabricius et al. 2021; Bhardwaj et al. 2021; Stassun & Torres 2021; Groenewegen 2023; Ding et al. 2025). An alternative route to Cepheid calibration that largely avoids the uncertainty of the parallax offset calibrates Cepheids in open clusters where the *Gaia* DR3 parallaxes are measured from fainter cluster stars ( $12 < G < 18$  mag), well within the range of the Lindgren et al. (2021) calibration, and achieves a 0.9% luminosity-scale precision consistent with that of the field Cepheids (Riess et al. 2022b; Cruz Reyes & Anderson 2023). The metallicity dependence of the period–luminosity relation has also been explored extensively (Breuval et al. 2022; Molinaro et al. 2023), although its magnitude remains debated, with recent claims of a negligible effect (Madore et al. 2025; Madore & Freedman 2026) challenged by evidence favouring the standard slope of  $\sim -0.2 \pm 0.1 \text{ mag dex}^{-1}$  (Breuval et al. 2025). However, this term has little leverage on  $H_0$ , with a change of  $\sim 0.2 \text{ km s}^{-1} \text{ Mpc}^{-1}$  for a  $0.1 \text{ mag dex}^{-1}$  change in slope due to the consistency of Cepheid metallicities along the distance ladder.

While many potential astrophysical systematics have been investigated, increasing attention has also focused on the statistical framework used to infer the Cepheid calibra-

tion and the treatment of selection effects. Several studies have explored the sensitivity of the distance ladder to modelling assumptions. For example, Efstathiou (2021) examined alternative implementations of the SH0ES analysis and discussed the impact of specific modelling choices; Kushnir & Sharon (2025) removed the requirement of a Cepheid period–luminosity relation; Bidenko et al. (2023) refit using a Gaussian process; Mörtzell et al. (2022) explored colour selection for Cepheids; see Verde et al. (2024) for a review. Subsequent analyses by the SH0ES team (Riess et al. 2022a, hereafter R22) have addressed these issues in updated treatments. Collectively, this body of work underscores that percent-level inference in the distance ladder requires careful and transparent treatment of statistical assumptions. On the Bayesian side, Cardona et al. (2017) marginalised over hyperparameters that down-weight outliers, Delgado et al. (2019) constructed a hierarchical model for period–luminosity relations from *Gaia* parallaxes, and Feeney et al. (2018) built a hierarchical model of the full distance ladder, inferring  $H_0$  end-to-end but adopting a uniform prior on distance modulus (thus failing to capture the intrinsically uniform-in-volume distribution of galaxies) and neglecting the selection function. None of these Bayesian approaches, however, incorporate a principled treatment of sample selection. Stiskalek et al. (2026) applied rigorous selection modelling to the geometric-anchor and Cepheid-host rungs of the distance ladder, but compressed the MW calibration into a single Gaussian constraint on the period–luminosity zero-point. Desmond et al. (2025) further showed, in a toy model and directly on the CosmicFlows-4 dataset (Tully et al. 2023), that neglecting selection within a Bayesian framework can significantly bias the inference of  $H_0$ .

We describe the MW, Large Magellanic Cloud (LMC), and N4258 Cepheid data in Section 2, and develop the Bayesian forward model in Section 3. Section 4 presents the fiducial posteriors and model validation, while Section 5 discusses the implications for  $H_0$ . Section 6 concludes. Throughout,  $\mathcal{N}(x | \mu, \sigma)$  denotes the univariate normal density with mean  $\mu$  and standard deviation  $\sigma$ , generalised to  $\mathcal{N}(x | \mu, \Sigma)$  for the multivariate case with covariance matrix  $\Sigma$ ;  $x \leftarrow \mathcal{N}(\mu, \sigma^2)$  indicates that  $x$  is drawn from the corresponding distribution;  $\Phi$  is the standard normal cumulative distribution function (CDF); and all logarithms are base-10.

## 2 GEOMETRIC AND CEPHEID DATA

We use the MW Cepheids compiled by R21, with *HST* photometry in the F555W, F814W, and F160W bands and *Gaia* EDR3 parallaxes (Gaia Collaboration et al. 2021). Of the 75 Cepheids in the R21 catalogue, seven lack *Gaia* EDR3 parallaxes that pass the RUWE or GOF quality cuts (CY Aur, DL Cas, RW Cam, SV Per, SY Nor, RX Cam, and U Aql) and are excluded. We further exclude S Vul and SV Vul, which were flagged as possible outliers in R21. Both exhibit significant secular period evolution, and as the longest-period, most massive Cepheids in the sample, their large angular diameters may also cause a shifting *Gaia* photocentre. This leaves 66 stars in the MW sample, the same sample analysed by R21 and HM26. Magnitudes are standardised

via the reddening-free Wesenheit magnitude  $m_H^W$  (Madore 1982).

The Cepheids were observed across two *HST* campaigns with distinct selection criteria given in R21: Cycle 22 (C22) targeted long-period Cepheids ( $P > 8$  days) within a distance range of  $\sim 6.6$  kpc, while Cycle 27 (C27) targeted nearby Cepheids at distances  $< 1.25$  kpc, with  $V > 6$  mag to avoid *Gaia* saturation. C27 was undertaken after the discovery of the *Gaia* parallax offset anomaly and the subsequent need for a broader range of Cepheid parallaxes to break degeneracies. Figure 2 shows the Galactocentric distribution of the combined sample, confirming that it traces the thin disk. Later in the analysis, we include additional Cepheid samples with geometric constraints: the LMC and N4258, taken from the SH0ES compilation of R22, as well as their host galaxy geometric distance measurements (Pietrzyński et al. 2019; Reid et al. 2019). *Gaia* parallaxes are subject to a global zero-point offset (Lindgren et al. 2021), which is a function of source magnitude, colour, and angular coordinate.  $\delta_\varpi$  denotes the residual parallax offset, i.e. that which may not be fully corrected by Lindgren et al. (2021), who refer to an uncertainty in their correction of several  $\mu\text{as}$ . For the regime of interest for Cepheids, the bright end of the Lindgren et al. (2021) calibrated range, we estimate the uncertainty in the correction to be  $\sigma \sim 10 \mu\text{as}$ . The reported parallax is  $\varpi_{\text{obs}} = 1/d - \delta_\varpi$ , where  $d$  is the distance; we treat  $\delta_\varpi$  as a free parameter throughout.

For each MW Cepheid, the R21 catalogue provides the Wesenheit apparent magnitude  $m_H^W$  with measurement uncertainty  $\sigma_m$ , the pulsation period  $P$ , a direct spectroscopic metallicity  $[\text{Fe}/\text{H}]$ , and the *Gaia* EDR3 parallax  $\varpi_{\text{obs}}$  with uncertainty  $\sigma_\varpi$ . We adopt the same  $[\text{Fe}/\text{H}]$  values as R21 and HM26 for consistency, but note the modest revisions reported by Bhardwaj et al. (2023). In Table 1 we summarise the observables that enter our model. The Wesenheit magnitude is constructed from the F555W, F814W, and F160W *HST* bands to minimise sensitivity to reddening, eliminating the need for individual extinction corrections. Periods are determined from decades of high-cadence monitoring and are effectively noise-free, especially in the MW and LMC, with uncertainties at the 1–2% level in  $\log P$  for more distant hosts. Metallicity uncertainties are dominated by systematic methodological differences rather than statistical errors, with a typical scatter of  $\sim 0.06$  dex.

The C22 parent population comprises known MW Cepheids drawn from historical variability catalogues such as the General Catalogue of Variable Stars (Samus’ et al. 2017), OGLE (Udalski et al. 1992), and Tammann et al. (2003), which impose an implicit completeness limit of  $V \lesssim 15$  mag. From this parent sample, three explicit cuts were applied for *HST* observation by SH0ES: a period cut  $P > 8$  days, an extinction cut  $A_H < 0.4$  mag, and a saturation cut  $V > 6$  mag to avoid *Gaia* detector saturation. Table 2 summarises the four datasets. The period cut is distance-independent, whereas the extinction and brightness cuts are distance-dependent. Of the  $\sim 70$  Cepheids in Tammann et al. (2003) satisfying these criteria, *HST* snapshot scheduling randomly selected 50 for observation. We assume this scheduling to be equivalent to random subsampling, which therefore requires no additional modelling. The  $V > 6$  mag cut excludes only the nearest Cepheids; only a single object (T Mon,  $V \approx 6.07$  mag) lies near this bound-

ary. The extinction cut  $A_H < 0.4$  mag preferentially removes distant Cepheids along dusty sightlines. To evaluate this extinction cut at arbitrary positions in the MW, we use a combination of the Bayestar19 three-dimensional dust map (Green et al. 2019), which covers declinations  $\delta > -30^\circ$ , and the Marshall et al. (2006) map for the inner MW where Bayestar19 lacks coverage.<sup>1</sup> Bayestar19 reddening is converted to  $A_H$  using  $R_H = 0.469$  (Green et al. 2019), while Marshall et al. (2006)  $A_{K_s}$  values are converted via  $A_H = 1.55 A_{K_s}$ . The formal implementation of this cut within the selection function is described in Section 3.4.

C27 targets nearby, high-parallax Cepheids to complement the more distant C22 sample, selecting those with photometric parallax  $\varpi_{\text{phot}} > 0.8$  mas and  $A_H < 0.6$  mag. The photometric parallax is given by

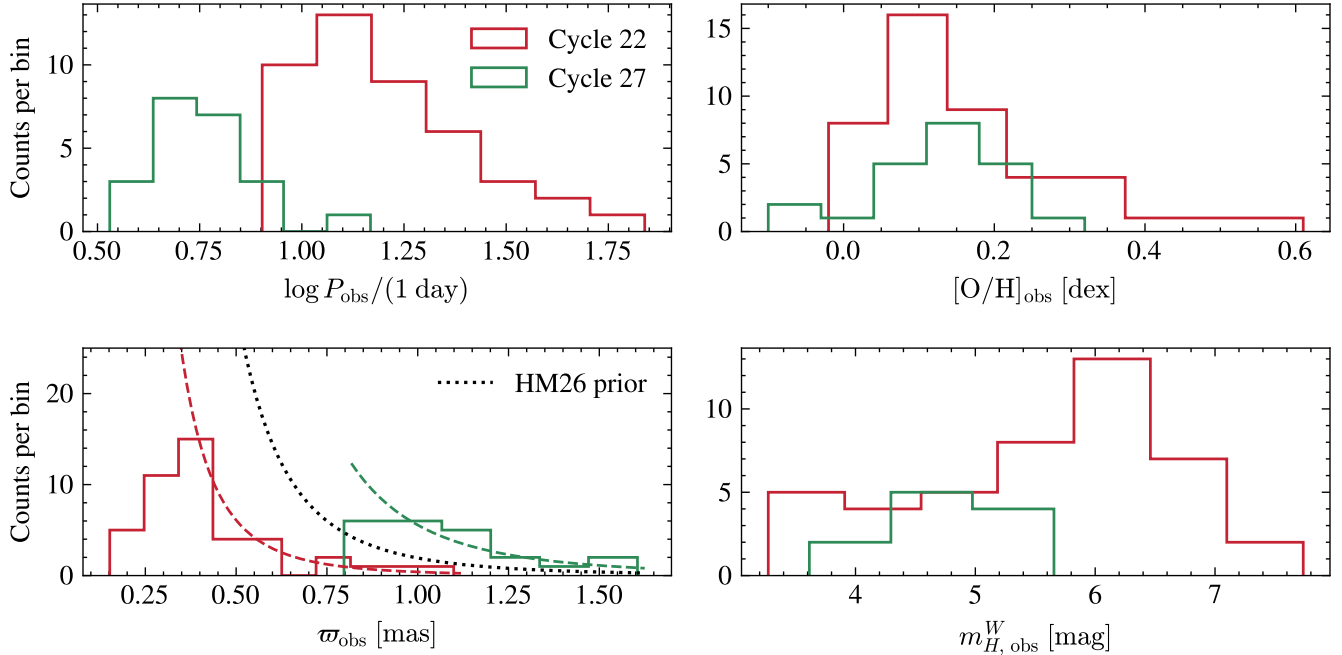
$$\log \frac{\varpi_{\text{phot}}}{1 \text{ mas}} = -0.2 \left[ m_H^W - \tilde{M}_{H,1}^W - \tilde{b}_W \left( \log \frac{P}{1 \text{ day}} - 1 \right) - \tilde{Z}_W [\text{Fe}/\text{H}] - 10 \right], \quad (1)$$

where  $\tilde{M}_{H,1}^W$ ,  $\tilde{b}_W$ , and  $\tilde{Z}_W$  are the period–luminosity zero-point, slope, and metallicity coefficient from Riess et al. (2016). This cut was applied to the predicted photometric parallax rather than the *Gaia* trigonometric parallax because the C27 proposal was written before *Gaia* DR3; the DR2 parallax uncertainties were roughly twice as large, making the photometric estimate more precise. However, we shall later treat this selection as a smooth lower limit on  $\varpi_{\text{obs}}$ .

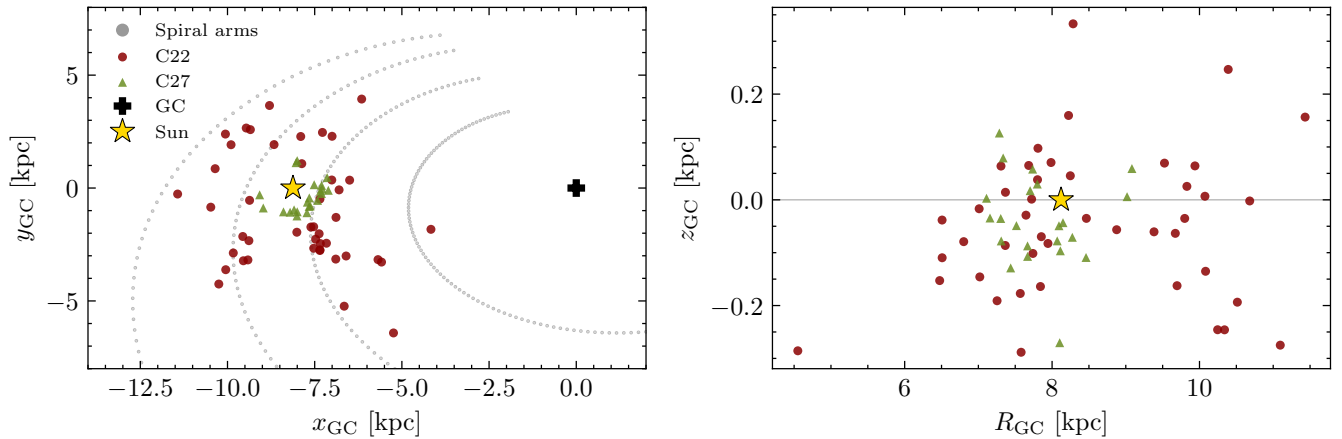
As an additional constraint on the *Gaia* parallax zero-point and the period–luminosity relation, we include two galaxies with independent geometric distance measurements. Pietrzyński et al. (2019) measured a distance modulus to the LMC of  $18.477 \pm 0.026$  mag from detached eclipsing binaries, while Reid et al. (2019) measured a distance modulus to N4258 of  $29.398 \pm 0.032$  mag from water megamaser kinematics. Both are adopted as geometric anchors for the Cepheid calibration, following the SH0ES programme (R22). We use 69 LMC and 443 N4258 Cepheids with *HST* photometry, observed using the same three-filter system as the MW sample, enabling a consistent calibration of the period–luminosity relation across these distance rungs. The R22 catalogue provides LMC and N4258 Cepheid Wesenheit apparent magnitudes together with per-galaxy covariance matrices  $\Sigma_j$  that account for crowding-induced photometric biases from sky background estimation and systematic uncertainties in the metallicity scale (section 2.1 of R22). For MW Cepheid metallicities we convert  $[\text{Fe}/\text{H}]$  to  $[\text{O}/\text{H}] = [\text{Fe}/\text{H}] + 0.06$ , following the R22 prescription based on Romaniello et al. (2022); the LMC and N4258 metallicities are already reported as  $[\text{O}/\text{H}]$ . The LMC sample uses a single metallicity value in accord with the finding by Romaniello et al. (2022) that all of the SH0ES Cepheids were consistent with the mean spectroscopic metallicity of the LMC field.

Figure 1 compares the distributions of  $\log P$ ,  $[\text{O}/\text{H}]$ ,  $\varpi_{\text{obs}}$ , and  $m_H^W$  for the C22 and C27 samples. The C27 selection on predicted parallax yields a sample of nearby

<sup>1</sup> Dust maps are queried using the `dustmaps` Python package (Green 2018).



**Figure 1.** Distributions of observed period ( $\log P$ ), metallicity ( $[O/H]$ ), *Gaia* EDR3 parallax ( $\varpi_{\text{obs}}$ ), and Wesenheit apparent magnitude ( $m_{H, \text{obs}}^W$ ) for the C22 (red) and C27 (green) Cepheid samples. Dashed lines in the parallax panel show the approximate expected  $\varpi_{\text{obs}}$  distribution for a uniform-in-volume prior  $\pi(d) \propto d^2$  between the minimum and maximum distances inferred from each campaign’s observed parallaxes (assuming  $\delta_{\varpi} = -0.01$  mas). The dashed curves are normalised to the observed sample size of each campaign. The black dotted line shows the same prior applied to the combined C22 + C27 sample treated as a single population, as done by [HM26](#) (shown with arbitrary normalisation).



**Figure 2.** Galactocentric distribution of the MW Cepheids (C22: dark red circles; C27: olive triangles), with distances from parallax inversion assuming  $\delta_{\varpi} = -0.01$  mas. *Left:* face-on projection with [Drimmel et al. \(2025\)](#) spiral arm traces (grey); the Sun and Galactic Centre (GC) positions are marked. The sample spans  $R_{GC} \approx 5-11$  kpc, concentrated in the solar neighbourhood. *Right:* edge-on view, confirming that the Cepheids trace the Galactic thin disk with height above the midplane  $|z_{GC}| \lesssim 0.3$  kpc.

Cepheids with systematically shorter periods and larger parallaxes, whereas the C22 sample extends to longer periods and smaller parallaxes. Both samples span a similar metallicity range,  $[O/H] \approx 0.0$  to  $0.4$  dex with a median of  $\sim 0.1$  dex. Each sample is a subset of known classical Cepheids from the GCVS catalogue. Both are confined to the MW disk and, even within the MW, cover only a limited range of distances due to selection: the parallax distributions in Fig. 1 lack Cepheids at small  $\varpi_{\text{obs}}$  relative to the expectation from

a volume-complete survey. The dashed lines in Fig. 1 show the parallax distribution expected from a uniform-in-volume prior (i.e., a sphere)  $\pi(d) \propto d^2$  spanning the distance range of each campaign, estimated from the observed parallaxes (assuming  $\delta_{\varpi} = -0.01$  mas). The observed histograms disagree with these reference curves because of the thin-disk MW geometry where Cepheids reside and sample selection. The discrepancy is particularly pronounced for C22. C27, by contrast, more closely resembles a volume-limited sam-

Symbol	Description	Populations
$m_H^W, \sigma_m$	Wesenheit Cepheid magnitude and uncertainty	All
$\log P_{\text{obs}}$	Cepheid pulsation period	All
$[\text{O}/\text{H}]_{\text{obs}}$	Cepheid (spectroscopic) metallicity	All
$\varpi_{\text{obs}}, \sigma_\varpi$	<i>Gaia</i> EDR3 parallax and its uncertainty	MW
$\ell, b$	Cepheid Galactic longitude and latitude	MW
$\tilde{\mu}_j, \sigma_{\mu,j}$	Host galaxy geometric distance modulus and its uncertainty	LMC, N4258
$\Sigma_j$	SH0ES Cepheid magnitude covariance matrix	LMC, N4258

**Table 1.** Summary of observables. “All” populations refer to all four datasets: C22, C27, LMC, and N4258.

Sample	Source	$N_{\text{Ceph}}$	Selection / anchor
C22	<i>HST</i> + <i>Gaia</i> EDR3	44	$P > 8$ days, $V > 6$ mag, $A_H < 0.4$ mag, $D \leq 6$ kpc
C27	<i>HST</i> + <i>Gaia</i> EDR3	22	$\varpi_{\text{phot}} > 0.8$ mas, $A_H < 0.6$ mag, $V > 6$ mag
LMC	<i>HST</i> (SH0ES)	69	DEB: $\mu = 18.477 \pm 0.026$ mag
N4258	<i>HST</i> (SH0ES)	443	Megamaser: $\mu = 29.398 \pm 0.032$ mag

**Table 2.** Summary of datasets.  $N_{\text{Ceph}}$  is the number of Cepheids in each sample. C22 and C27 are from R21; LMC and N4258 are from R22. Counts are after excluding 9 stars (7 lacking *Gaia* EDR3 parallaxes passing GOF/RUWE quality cuts, 2 outliers) from the original 75. For the LMC and N4258, only *HST* photometry is used. Geometric anchors: LMC detached eclipsing binary distance from Pietrzyński et al. (2019); N4258 megamaser distance from Reid et al. (2019).

ple, albeit local, because of its parallax cut, which imposes an effective upper distance limit. Applying a single uniform-volume prior over the combined distance range of both campaigns, as done by HM26, who do not split the sample, would extend this mismatch further as shown by the black dotted line. We shall compare to their work in Section 5.2. This incompleteness—driven by the selection criteria described above—must be accounted for in the inference, and motivates the forward-modelling approach of Section 3.

The necessity of restricting the distance prior to match the sample boundary even for nominally volume-limited samples—where all sources with true distance below some threshold are observed—was recently stressed by Desmond et al. (2025); neglecting this restriction biases the inferred Hubble constant in mock distance ladder examples. Stiskalek et al. (2026) applied rigorous selection modelling to a two-rung distance ladder.

### 3 BAYESIAN FORWARD MODEL

We construct a Bayesian forward model to jointly infer the period–luminosity relation parameters, the parallax zero-point offset  $\delta_\varpi$ , and per-star distances, broadly following the forward-modelling framework of Stiskalek et al. (2026). Our approach differs from that of R21, who optimise in paral-

lax space using model (i.e., photometric) parallaxes derived from observed magnitudes and periods, in that we forward-model the Cepheid observables directly by sampling per-star distances as latent variables. The data consist of Wesenheit apparent magnitudes  $m_H^W$  from *HST*, pulsation periods  $P$ , spectroscopic metallicities  $[\text{O}/\text{H}]$ , and *Gaia* EDR3 parallaxes  $\varpi$  for the 66 MW Cepheids described in Section 2, together with the host geometric distance and Cepheid photometry in the LMC and N4258 (Table 1). The model comprises four Cepheid populations, all consistently measured with *HST*: the two MW campaigns C22 and C27, and the LMC and N4258. All four share the period–luminosity relation parameters ( $M_{H,1}^W, b_W, Z_W$ ), while the two MW campaigns share the parallax zero-point offset  $\delta_\varpi$ . Each population  $p$  has independent period distribution hyperparameters, and all populations except the LMC additionally have independent metallicity distribution hyperparameters (Eq. 7). For the LMC, the catalogued metallicities are used as fixed covariates (Section 3.3). The two MW campaigns are additionally modelled with independent intrinsic scatters  $\sigma_{\text{int}}^{\text{C22}}$  and  $\sigma_{\text{int}}^{\text{C27}}$ ; for the LMC and N4258, an intrinsic scatter of 0.06 mag is already included in the SH0ES-reported covariance matrices  $\Sigma_j$ , and we do not recalibrate it. As we find, this 0.06 mag scatter closely matches our inferred values for the MW campaigns. We denote the full set of global parameters  $\Lambda$ ; the directed acyclic graph of the model is shown in Fig. 3.

#### 3.1 Priors

We adopt broad normal priors on the period–luminosity parameters  $M_{H,1}^W, b_W$ , and  $Z_W$ , centred approximately on the R21 fiducial values. Since both the priors and posteriors are near-Gaussian, the fractional information contributed by the prior is  $\sigma_{\text{post}}^2/\sigma_{\text{prior}}^2$ , where  $\sigma_{\text{post}}$  is the posterior width reported in Section 4. This evaluates to at most 1% for  $M_{H,1}^W, b_W$ , and  $Z_W$  in the fiducial model, so any double-counting with R21 is negligible. Following R21, we sample the zero-point offset  $\delta_\varpi$  from a normal prior. Similarly, the intrinsic scatters  $\sigma_{\text{int}}^{\text{C22}}$  and  $\sigma_{\text{int}}^{\text{C27}}$  are each sampled independently from a truncated normal prior.

For the  $i^{\text{th}}$  MW Cepheid, the distance  $d_i$  is drawn from a Galactic disk prior that models Cepheids as tracing a thin disk. The joint density over position  $(d, \ell, b)$  is

$$\pi(d, \ell, b) = \frac{1}{\mathcal{Z}_V} d^2 \exp\left(-\frac{R_{\text{GC}}}{R_d}\right) \exp\left(-\frac{|z|}{z_d}\right), \quad (2)$$

where  $R_{\text{GC}}$  is the Galactocentric radius,  $z$  the height above the midplane,  $R_d$  the disk scale length,  $z_d$  the scale height, and  $\mathcal{Z}_V = \int dd d\ell db \cos b d^2 \exp(-R_{\text{GC}}/R_d) \exp(-|z|/z_d)$  is the volume prior normalisation. The factor  $d^2$  arises from the volume element in spherical coordinates. Galactocentric coordinates follow from heliocentric distance  $d$  and Galactic longitude and latitude  $(\ell, b)$  as

$$R_{\text{GC}} = \sqrt{(R_\odot - d \cos b \cos \ell)^2 + (d \cos b \sin \ell)^2}, \quad (3)$$

$$z = d \sin b, \quad (4)$$

where  $R_\odot = 8.122$  kpc is the solar Galactocentric distance (GRAVITY Collaboration 2019).

We adopt  $R_d = 2.5$  kpc and  $z_d = 0.1$  kpc, consistent with  $R_d = 2.30 \pm 0.09$  kpc measured by Bobylev & Bajkova

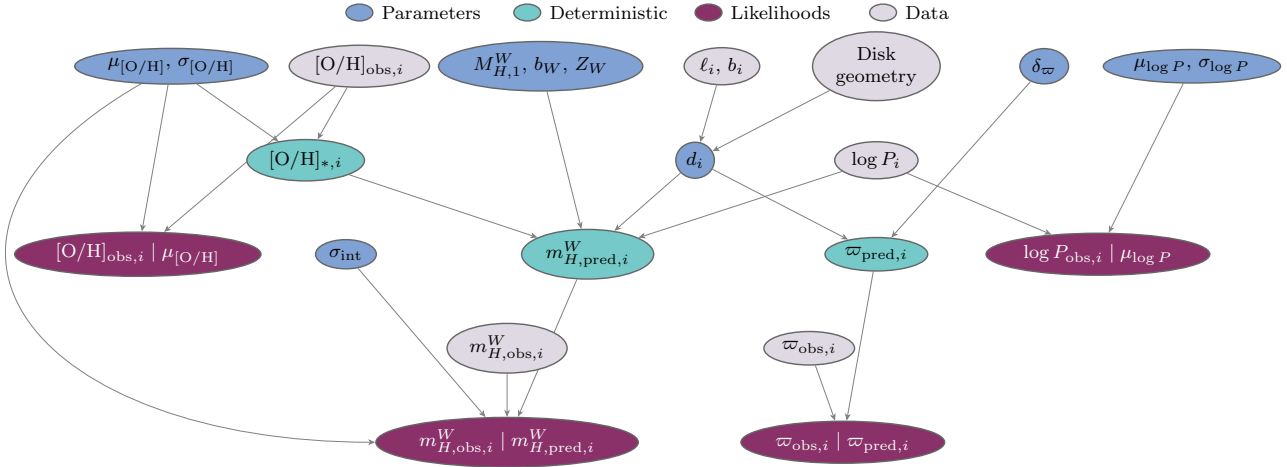


**Figure 3.** Directed acyclic graph of the forward model for a single MW campaign. Blue nodes denote parameters drawn from priors, grey nodes observed data, teal nodes deterministic functions of their parents, and purple nodes the likelihoods. The period hyperprior ( $\mu_{\log P}$ ,  $\sigma_{\log P}$ ) connects only to the period likelihood, which evaluates the Gaussian period prior at the observed  $\log P_i$  (second factor of Eq. 40); it does not enter the magnitude likelihood, since the delta-function marginalisation over the true period replaces it with the observed value. The metallicity hyperprior ( $\mu_{[\text{O}/\text{H}]}$ ,  $\sigma_{[\text{O}/\text{H}]}$ ) connects to both a standalone metallicity likelihood and the magnitude likelihood. The observed  $\ell_i$  and  $b_i$  enter as fixed inputs with negligible measurement uncertainty. When multiple campaigns are modelled jointly, the period–luminosity parameters ( $M_{H,1}^W$ ,  $b_W$ ,  $Z_W$ ) and parallax offset  $\delta_\varpi$  are shared across all populations, while the period and metallicity hyperparameters and intrinsic scatter are independent per campaign. Selection modelling, described in Section 3.4, is not shown here.

(2021) for young ( $< 120$  Myr) Cepheids and with Nunnari et al. (2025); the adopted  $z_d$  is larger than the Bobylev & Bajkova (2021) value of  $75 \pm 5$  pc, but our results are insensitive to it. Varying  $R_d$  and  $z_d$  within observationally supported bounds has a negligible effect on the inferred parameters. The more fundamental point, whether the disk prior matters relative to a uniform-in-volume prior, is addressed in Section 4, where we show that replacing the disk prior with a uniform-in-volume prior while retaining the selection model shifts  $M_{H,1}^W$  by only 0.002 mag; the dominant effect comes from self-consistently modelling the selection function rather than from the choice of distance prior. The prior is truncated to  $[d_{\min}, d_{\max}]$  and normalised numerically per sightline via Simpson’s rule, where  $d_{\min} = 0.1$  kpc and  $d_{\max} = 8.5$  kpc for C22 and  $d_{\max} = 2.0$  kpc for C27. These upper limits are never reached by the posterior and have no impact on the inference, provided they are sufficiently large. For the LMC and N4258, we sample the distance  $d_j$  to each host from a uniform-in-volume prior.

The angular positions of observed Cepheids are known, but computing the detection probability of Section 3.4 requires marginalising over the angular position  $\Omega = (\ell, b)$  on the sky, since the normalisation integral extends over all positions where a Cepheid *could* have been detected. The conditional prior on distance given sky position is  $\pi(d | \Omega) = \pi(d, \Omega) / \pi(\Omega)$ , where the population angular distribution follows from marginalising Eq. (2) over distance,

$$\pi(\Omega) = \frac{\mathcal{Z}(\Omega)}{\mathcal{Z}_V}, \quad (5)$$

where

$$\mathcal{Z}(\Omega) \equiv \int dd d^2 \exp\left(-\frac{R_{\text{GC}}}{R_d}\right) \exp\left(-\frac{|z|}{z_d}\right), \quad (6)$$

which depends on the disk model parameters ( $R_d$ ,  $z_d$ ) and is largest in directions where the disk column density is highest. The true pulsation period and metallicity of each Cepheid are treated as latent variables drawn from population-specific Gaussian distributions,

$$\begin{aligned} \log P &\leftrightarrow \mathcal{N}(\mu_{\log P}^p, (\sigma_{\log P}^p)^2), \\ [\text{O}/\text{H}] &\leftrightarrow \mathcal{N}(\mu_{[\text{O}/\text{H}]}^p, (\sigma_{[\text{O}/\text{H}]}^p)^2), \end{aligned} \quad (7)$$

where  $p$  denotes the population to which the Cepheid belongs. Each population has an independent set of period hyperparameters ( $\mu_{\log P}^p$ ,  $\sigma_{\log P}^p$ ); the metallicity hyperparameters ( $\mu_{[\text{O}/\text{H}]}^p$ ,  $\sigma_{[\text{O}/\text{H}]}^p$ ) are sampled independently for all populations except the LMC, for which the catalogued metallicities are treated as fixed inputs since the SH0ES catalogue reports only a single metallicity value for LMC Cepheids (Section 3.3). The means are sampled with uniform priors and the standard deviations with half-normal priors. The period and metallicity distributions are assumed independent. Such Gaussian hyperpriors have been found to yield unbiased regression even in cases where the population distribution is non-Gaussian (Bartlett & Desmond 2023). In the remainder of this section, we suppress the population superscript  $p$  for brevity; all population-dependent quantities are understood to carry it.

### 3.2 Deterministic transformations

Given the sampled global parameters, per-star distances, and latent true periods and metallicities, we compute the predicted observables deterministically. The period–luminosity relation gives the absolute Wesenheit magnitude

of the  $i^{\text{th}}$  Cepheid as

$$M_{H,i}^W = M_{H,1}^W + b_W \left( \log \frac{P_i}{1 \text{ day}} - 1 \right) + Z_W [\text{O}/\text{H}]_i, \quad (8)$$

where  $P_i$  is the latent true period and  $[\text{O}/\text{H}]_i$  the latent true metallicity; the wavelength dependence of  $Z_W$  is discussed in Breuval et al. (2022). The predicted apparent magnitude then follows from the distance modulus,

$$m_{H,\text{pred},i}^W(d_i, \mathbf{\Lambda}) = M_{H,i}^W + \mu(d_i), \quad (9)$$

$$\mu(d) = 5 \log_{10}(d/\text{kpc}) + 10, \quad (10)$$

and the predicted parallax is

$$\varpi_{\text{pred},i} = \frac{1 \text{ mas}}{d_i/\text{kpc}} - \delta_{\varpi}, \quad (11)$$

where  $\delta_{\varpi}$  is the *Gaia* parallax zero-point offset. For the LMC and N4258, the predicted apparent magnitudes follow from the same period–luminosity relation, with all Cepheids in galaxy  $j$  placed at distance  $d_j$ .

### 3.3 Likelihoods

For each MW Cepheid, the observed Wesenheit magnitude and *Gaia* EDR3 parallax are compared to their predicted values. The magnitude likelihood for the  $i^{\text{th}}$  Cepheid, conditioned on the true period  $\log P_i$  and metallicity  $[\text{O}/\text{H}]_i$ , is

$$\begin{aligned} \mathcal{L}(m_{H,\text{obs},i}^W | d_i, \log P_i, [\text{O}/\text{H}]_i, \mathbf{\Lambda}) \\ = \mathcal{N}\left(m_{H,\text{obs},i}^W | m_{H,\text{pred},i}^W, \sqrt{\sigma_{m,i}^2 + (\sigma_{\text{int}}^{c_i})^2}\right), \end{aligned} \quad (12)$$

where  $\sigma_{m,i}$  is the photometric uncertainty and  $\sigma_{\text{int}}^{c_i}$  the intrinsic scatter for campaign  $c_i \in \{\text{C22}, \text{C27}\}$ . The parallax likelihood is

$$\mathcal{L}(\varpi_{\text{obs},i} | d_i, \mathbf{\Lambda}) = \mathcal{N}(\varpi_{\text{obs},i} | \varpi_{\text{pred},i}, \sigma_{\varpi,i}), \quad (13)$$

where  $\sigma_{\varpi,i}$  is the reported *Gaia* parallax uncertainty.

The period measurement uncertainties are negligibly small, so the period likelihood is effectively a delta function,

$$\mathcal{L}(\log P_{\text{obs},i} | \log P_i) \approx \delta(\log P_{\text{obs},i} - \log P_i). \quad (14)$$

For the metallicity, individual measurement uncertainties are rarely reported; the dominant errors are methodological and approximately constant across the sample. We therefore adopt a Gaussian likelihood with a fixed measurement uncertainty  $\epsilon_{[\text{O}/\text{H}]} = 0.06$  dex, consistent with the  $\sim 0.05$  dex systematic scale uncertainty adopted by Gieren et al. (2018), the  $\sim 0.07$  dex propagated measurement error reported by Romaniello et al. (2022), and the  $\lesssim 0.05$  dex precision achieved in the homogeneous reanalysis of da Silva et al. (2022). The exact value has negligible impact on the inference, as it enters only through the precision-weighted combination with the population scatter  $\sigma_{[\text{O}/\text{H}]}$ .

$$\mathcal{L}([\text{O}/\text{H}]_{\text{obs},i} | [\text{O}/\text{H}]_i) = \mathcal{N}([\text{O}/\text{H}]_{\text{obs},i} | [\text{O}/\text{H}]_i, \epsilon_{[\text{O}/\text{H}]}) \quad (15)$$

where  $\epsilon_{[\text{O}/\text{H}]}$  denotes the measurement uncertainty, distinct from the population scatter  $\sigma_{[\text{O}/\text{H}]}$  of Eq. (7).

Similarly, the sky position of each Cepheid is measured effectively without error, so the likelihood of the observed angular position is a delta function,  $\mathcal{L}(\mathbf{\Omega}_{\text{obs}} | \mathbf{\Omega}) = \delta(\mathbf{\Omega} - \mathbf{\Omega}_{\text{obs}})$ . The full prior on the star’s three-dimensional position

is  $\pi(d, \mathbf{\Omega}) = \pi(d | \mathbf{\Omega}) \pi(\mathbf{\Omega})$ —Eqs. (2) and (5); integrating over the true sky position against the delta function evaluates  $\pi(\mathbf{\Omega})$  at  $\mathbf{\Omega}_{\text{obs}}$ . Since  $\pi(d | \mathbf{\Omega}) = \pi(d, \mathbf{\Omega})/\pi(\mathbf{\Omega})$ , the factor  $\pi(\mathbf{\Omega}_{\text{obs}})$  from the prior cancels with the denominator of the conditional, leaving simply  $\pi(d, \mathbf{\Omega}_{\text{obs}}) = \varrho(d, \mathbf{\Omega}_{\text{obs}})/\mathcal{Z}_V$ , where

$$\varrho(d, \mathbf{\Omega}) \equiv d^2 \exp\left(-\frac{R_{\text{GC}}}{R_d}\right) \exp\left(-\frac{|z|}{z_d}\right) \quad (16)$$

is the unnormalised disk density. The remaining global normalisation  $\mathcal{Z}_V$  cancels against the selection term, which we will introduce in Section 3.4.

The true period and metallicity are nuisance latent parameters that can be marginalised analytically. Combining the measurement likelihoods with the Gaussian population prior of Eq. (7), the joint marginalised likelihood is

$$\begin{aligned} \mathcal{L}^{\text{marg}}(m_{H,\text{obs},i}^W, \log P_{\text{obs},i}, [\text{O}/\text{H}]_{\text{obs},i} | d_i, \mathbf{\Lambda}) \\ = \int d \log P_i d [\text{O}/\text{H}]_i \mathcal{L}(m_{H,\text{obs},i}^W | d_i, \log P_i, [\text{O}/\text{H}]_i, \mathbf{\Lambda}) \\ \times \mathcal{L}(\log P_{\text{obs},i} | \log P_i) \mathcal{L}([\text{O}/\text{H}]_{\text{obs},i} | [\text{O}/\text{H}]_i) \\ \times \pi(\log P_i | \mathbf{\Lambda}) \pi([\text{O}/\text{H}]_i | \mathbf{\Lambda}). \end{aligned} \quad (17)$$

The delta-function period likelihood of Eq. (14) collapses the integral over  $\log P_i$ , setting  $\log P_i = \log P_{\text{obs},i}$  and leaving behind the period prior  $\pi(\log P_{\text{obs},i} | \mathbf{\Lambda})$ . The true metallicity  $[\text{O}/\text{H}]_i$  enters the magnitude likelihood linearly through the  $Z_W [\text{O}/\text{H}]_i$  term of the period–luminosity relation, while both the metallicity likelihood and population prior are Gaussian; the three factors are jointly Gaussian in  $[\text{O}/\text{H}]_i$  and integrate analytically to give

$$\begin{aligned} \mathcal{L}^{\text{marg}}(m_{H,\text{obs},i}^W, \log P_{\text{obs},i}, [\text{O}/\text{H}]_{\text{obs},i} | d_i, \mathbf{\Lambda}) \\ = \mathcal{N}\left(m_{H,\text{obs},i}^W | m_{H,\text{pred},i}^W(d_i, \log P_{\text{obs},i}, [\text{O}/\text{H}]_{\star,i}), \sigma_{1,i}\right) \\ \times \mathcal{N}(\log P_{\text{obs},i} | \mu_{\log P}, \sigma_{\log P}) \\ \times \mathcal{N}\left([\text{O}/\text{H}]_{\text{obs},i} | \mu_{[\text{O}/\text{H}]}, \sqrt{\epsilon_{[\text{O}/\text{H}]}^2 + \sigma_{[\text{O}/\text{H}]}^2}\right), \end{aligned} \quad (18)$$

where  $[\text{O}/\text{H}]_{\star,i}$  is the effective metallicity, obtained as the precision-weighted mean of the observed value and the population mean,

$$[\text{O}/\text{H}]_{\star,i} = \tilde{\sigma}_{[\text{O}/\text{H}]}^2 \left( \frac{[\text{O}/\text{H}]_{\text{obs},i}}{\epsilon_{[\text{O}/\text{H}]}^2} + \frac{\mu_{[\text{O}/\text{H}]}}{\sigma_{[\text{O}/\text{H}]}^2} \right), \quad (19)$$

with posterior precision  $\tilde{\sigma}_{[\text{O}/\text{H}]}^{-2} = \epsilon_{[\text{O}/\text{H}]}^{-2} + \sigma_{[\text{O}/\text{H}]}^{-2}$ . The total variance is  $\sigma_{1,i}^2 = \sigma_{m,i}^2 + (\sigma_{\text{int}}^{c_i})^2 + Z_W^2 \tilde{\sigma}_{[\text{O}/\text{H}]}^2$ . The second factor in Eq. (18) is the period prior evaluated at the observed period, which constrains  $\mu_{\log P}$  and  $\sigma_{\log P}$ ; the third is the marginalised metallicity likelihood, which constrains  $\mu_{[\text{O}/\text{H}]}$  and  $\sigma_{[\text{O}/\text{H}]}$ . The marginalised per-star likelihood is therefore

$$\begin{aligned} \mathcal{L}_i = \mathcal{L}^{\text{marg}}(m_{H,\text{obs},i}^W, \log P_{\text{obs},i}, [\text{O}/\text{H}]_{\text{obs},i} | d_i, \mathbf{\Lambda}) \\ \times \mathcal{N}(\varpi_{\text{obs},i} | \varpi_{\text{pred},i}, \sigma_{\varpi,i}). \end{aligned} \quad (20)$$

For  $j \in \{\text{LMC}, \text{N4258}\}$ , the geometric distance modulus constrains the galaxy distance via

$$\mathcal{L}(\tilde{\mu}_j | \mu_j) = \mathcal{N}(\tilde{\mu}_j | \mu_j, \sigma_{\mu,j}), \quad (21)$$

where  $\tilde{\mu}_j$  is the measured geometric distance modulus,  $\sigma_{\mu,j}$  its uncertainty, and  $\mu_j = \mu(d_j)$  is the distance modulus corresponding to the sampled galaxy distance  $d_j$ . The anchor

Cepheid photometry is modelled as a multivariate normal:

$$\mathcal{L}(\mathbf{m}_{H,j}^W | \mu_j, \mathbf{\Lambda}) = \mathcal{N}(\mathbf{m}_{H,j}^W | \mathbf{M}_{H,j}^W + \mu_j, \mathbf{\Sigma}_j), \quad (22)$$

where  $\mathbf{M}_{H,j}^W$  is the vector of predicted absolute magnitudes from the period–luminosity relation and  $\mathbf{\Sigma}_j$  is the SH0ES-reported covariance matrix. As for the MW Cepheids, the delta-function period likelihood sets  $\log P_k = \log P_{\text{obs},k}$  in each predicted absolute magnitude, leaving behind the period prior factors  $\pi(\log P_{\text{obs},k} | \mathbf{\Lambda})$ . For N4258, which has spectroscopic [O/H] measurements, the true metallicities are marginalised as in Eq. (18), adopting  $\epsilon_{[\text{O}/\text{H}]} = 0.06$  dex. Each Cepheid’s predicted absolute magnitude is evaluated at the effective metallicity  $[\text{O}/\text{H}]_{*,k}$  of Eq. (19), and the marginalisation adds  $Z_W^2 \tilde{\sigma}_{[\text{O}/\text{H}]}^2$  to the diagonal of the covariance. Because each Cepheid’s magnitude depends linearly on its own metallicity, and the per-star metallicity posteriors are conditionally independent given the population hyperparameters, the off-diagonal structure of  $\mathbf{\Sigma}_j$  is unchanged. The marginalised anchor Cepheid likelihood is therefore

$$\begin{aligned} \mathcal{L}_j^{\text{marg}} = & \mathcal{N}\left(\mathbf{m}_{H,j}^W | \mathbf{M}_{H,j}^W(\log \mathbf{P}_{\text{obs}}, [\text{O}/\text{H}]_{*,j}) + \mu_j, \right. \\ & \left. \mathbf{\Sigma}_j + Z_W^2 \tilde{\sigma}_{[\text{O}/\text{H}]}^2 \mathbf{I}\right) \\ & \times \prod_{k=1}^{N_j} \mathcal{N}(\log P_{\text{obs},k} | \mu_{\log P}, \sigma_{\log P}) \\ & \times \mathcal{N}\left([\text{O}/\text{H}]_{\text{obs},k} | \mu_{[\text{O}/\text{H}]}, \sqrt{\epsilon_{[\text{O}/\text{H}]}^2 + \sigma_{[\text{O}/\text{H}]}^2}\right), \quad (23) \end{aligned}$$

where  $N_j$  is the number of Cepheids in galaxy  $j$ , and  $\log \mathbf{P}_{\text{obs}}$  and  $[\text{O}/\text{H}]_{*,j}$  denote the vectors of observed periods and effective metallicities for those Cepheids. For the LMC, the catalogue reports a single spectroscopic metallicity value (Section 2); we therefore treat it as a fixed covariate in the predicted absolute magnitudes, dropping the metallicity marginalisation and the covariance contribution  $Z_W^2 \tilde{\sigma}_{[\text{O}/\text{H}]}^2 \mathbf{I}$  from Eq. (23), and do not infer the population hyperparameters  $\mu_{[\text{O}/\text{H}]}$  and  $\sigma_{[\text{O}/\text{H}]}$  for the LMC.

Both anchor catalogues are truncated at  $\log P_{\text{cut}} = -0.3$  (i.e.  $P_{\text{cut}} \approx 0.5$  day), excluding short-period Cepheids. Following the same selection framework as for the MW campaigns (Section 3.4), the selection-adjusted anchor likelihood is Eq. (23) divided by the detection probability—the probability that a Cepheid drawn from the population prior satisfies the period cut. The per-star period prior in Eq. (23) remains the full Gaussian  $\mathcal{N}(\log P_{\text{obs},k} | \mu_{\log P}, \sigma_{\log P})$ ; the per-star selection weight is unity for all observed Cepheids (since they all satisfy  $\log P_{\text{obs},k} > \log P_{\text{cut}}$ ), and only the normalisation factor contributes. Because there is no magnitude selection for the LMC and N4258, the integral of the multivariate magnitude likelihood over  $\mathbf{m}$  evaluates to unity irrespective of the covariance  $\mathbf{\Sigma}_j$ , and the detection probability reduces to

$$\begin{aligned} p(S = 1 | \mathbf{\Lambda}) &= \int_{\log P_{\text{cut}}}^{\infty} \mathcal{N}(\log P | \mu_{\log P}, \sigma_{\log P}) d \log P \\ &= \Phi\left(\frac{\mu_{\log P} - \log P_{\text{cut}}}{\sigma_{\log P}}\right). \quad (24) \end{aligned}$$

The selection-adjusted anchor likelihood is therefore Eq. (23) divided by  $p(S = 1 | \mathbf{\Lambda})^{N_j}$ .

### 3.4 Selection modelling

Both the C22 and C27 samples are subject to selection criteria. We account for these following the framework of Kelly (2007) (recently applied and extended by Stiskalek et al. 2026), which introduces two terms: a per-star selection weight and a normalisation factor. We model each selection criterion as a smooth cut on some observable  $x$ , with transition width  $w_x$  (the sharp period cut of Eq. (24) is recovered in the  $w_x \rightarrow 0$  limit). The selection function for a lower or upper threshold is, respectively,

$$\begin{aligned} \mathcal{S}_{\text{low}}(x) &= \Phi\left(\frac{x - x_{\text{min}}}{w_x}\right), \\ \mathcal{S}_{\text{high}}(x) &= \Phi\left(\frac{x_{\text{max}} - x}{w_x}\right). \quad (25) \end{aligned}$$

The selection function enters the posterior of Eq. (47) through two terms. The first is the per-star selection weight, given by Eq. (25) evaluated at the observed catalogue values. For example, for a star with observed magnitude  $m$  and an upper limit at  $m_{\text{max}}$ , the per-star selection weight is

$$\mathcal{S}(m) = \Phi\left(\frac{m_{\text{max}} - m}{w_m}\right). \quad (26)$$

The second term is a normalisation factor  $[p(S = 1 | \mathbf{\Lambda})]^{-n_p}$ , where  $n_p$  is the number of observed stars and  $p(S = 1 | \mathbf{\Lambda})$  is the marginalised detection probability. This is obtained by integrating the selection function weighted by the likelihood and prior over all observed and latent variables:

$$p(S = 1 | \mathbf{\Lambda}) = \int d\mathbf{x} d\boldsymbol{\theta} \mathcal{S}(\mathbf{x}) \mathcal{L}(\mathbf{x} | \boldsymbol{\theta}, \mathbf{\Lambda}) \pi(\boldsymbol{\theta} | \mathbf{\Lambda}), \quad (27)$$

where  $\mathbf{x}$  denotes the observed quantities,  $\boldsymbol{\theta}$  the per-source latent parameters (such as distance),  $\mathcal{L}(\mathbf{x} | \boldsymbol{\theta}, \mathbf{\Lambda})$  the likelihood of the observables, and  $\pi(\boldsymbol{\theta} | \mathbf{\Lambda})$  the prior, which may depend on some of the global parameters.

For the Cepheid problem, we consider the per-star selection weight of Eq. (26) to comprise cuts on up to four observables: the Wesenheit magnitude  $m_{H,\text{obs}}^W$ , the parallax  $\varpi_{\text{obs}}$ , the pulsation period  $\log P_{\text{obs}}$ , and the  $H$ -band extinction  $A_H$ . We assume no selection on metallicity, though one could be straightforwardly included. We model the magnitude selection as an effective cut in the Wesenheit band; the underlying photometric criteria are not strictly in Wesenheit, but the Wesenheit magnitude is directly predictable from the period–luminosity relation, making this considerably easier in practice (see Section 5.4 for further discussion). The corresponding marginalised detection probability of Eq. (27) is

$$\begin{aligned} p(S = 1 | \mathbf{\Lambda}) &= \int d\boldsymbol{\Omega} dd dm d\varpi \\ &\times d \log P d \log P_{\text{obs}} d[\text{O}/\text{H}] d[\text{O}/\text{H}]_{\text{obs}} \\ &\times \mathcal{S}(m, \varpi, \log P_{\text{obs}}, A_H(d, \boldsymbol{\Omega})) \\ &\times \mathcal{L}(m | d, \log P, [\text{O}/\text{H}], \mathbf{\Lambda}) \mathcal{L}(\varpi | d, \mathbf{\Lambda}) \\ &\times \mathcal{L}(\log P_{\text{obs}} | \log P) \mathcal{L}([\text{O}/\text{H}]_{\text{obs}} | [\text{O}/\text{H}]) \\ &\times \pi(d, \boldsymbol{\Omega}) \pi(\log P, [\text{O}/\text{H}] | \mathbf{\Lambda}), \quad (28) \end{aligned}$$

where  $\boldsymbol{\Omega}$  denotes the angular position on the sky,  $m \equiv m_H^W$  the Wesenheit magnitude,  $\varpi$  the parallax, and  $A_H(d, \boldsymbol{\Omega})$  the line-of-sight (LOS)  $H$ -band extinction obtained from a combination of the **Bayestar19** three-dimensional dust

Symbol	Description	Populations	Prior / Value
<b>Shared inferred parameters</b>			
$M_{H,1}^W$	Period–luminosity relation zero-point at $\log P = 1$	All	$\mathcal{N}(-5.9, 0.5)$
$b_W$	Period–luminosity relation slope	All	$\mathcal{N}(-3.3, 0.5)$
$Z_W$	Metallicity coefficient	All	$\mathcal{N}(-0.2, 0.5)$
$\delta_\varpi$	<i>Gaia</i> parallax zero-point offset	C22, C27	$\mathcal{N}(0, 10)$ , $\delta_\varpi \in [-100, 100]$ $\mu\text{as}$
<b>Per-population inferred parameters</b>			
$\sigma_{\text{int}}^p$	Intrinsic scatter	C22, C27	$\mathcal{N}(0.06, 0.03)$ , $\sigma_{\text{int}}^p > 0.01$ mag
$\mu_{\log P}^p$	Period distribution mean	All	$\mathcal{U}(-2.5, 2.5)$
$\sigma_{\log P}^p$	Period distribution std. dev.	All	$\mathcal{N}(0, 1)$ , $\sigma_{\log P}^p > 0$
$\mu_{[\text{O}/\text{H}]}^p$	Metallicity distribution mean	C22, C27, N4258	$\mathcal{U}(-0.5, 0.5)$
$\sigma_{[\text{O}/\text{H}]}^p$	Metallicity distribution std. dev.	C22, C27, N4258	$\mathcal{N}(0, 1)$ , $\sigma_{[\text{O}/\text{H}]}^p > 0$
$d_j$	Host galaxy distance	LMC, N4258	$\propto d_j^2$
$\varpi_{\text{min}}$	Effective parallax lower limit	C22	$\mathcal{U}(0.1, 0.6)$ mas
$m_{H,\text{max}}^W$	Effective magnitude upper limit	C22	$\mathcal{U}(6, 10)$ mag
$m_{H,\text{min}}^W$	Effective magnitude lower limit	C27	$\mathcal{U}(2, 4)$ mag
<b>Per-star inferred parameters</b>			
$d_i$	Distance to each Cepheid	C22, C27	Disk prior (Eq. 2)
<b>Fixed parameters</b>			
$\varpi_{\text{min}}$	Parallax lower limit	C27	0.8 mas
$w_\varpi$	Transition width	C22, C27	C22: 0.1 mas; C27: 0.05 mas
$w_m$	Transition width	C22, C27	C22: 0.5 mag; C27: 0.1 mag
$\log P_{\text{min}}$	Period lower limit	C22	0.90
$w_{\log P}$	Transition width	C22	0.01
$A_{H,\text{max}}$	Extinction upper limit (optional)	C22	0.4 mag
$w_{A_H}$	Transition width (optional)	C22	0.1 mag
$\log P_{\text{cut}}$	Period truncation	LMC, N4258	-0.3
$\epsilon_{[\text{O}/\text{H}]}$	Metallicity measurement uncertainty	All	0.06 dex
$R_d, z_d$	Disk scale length and height (Eq. 2)	C22, C27	2.5, 0.1 kpc

**Table 3.** Model parameters. “All” refers to C22, C27, LMC, and N4258. Per-population quantities (superscript  $p$ ) are sampled independently for each population. In total, the model has 91 inferred parameters: 4 shared, 21 per-population (the LMC contributes only period hyperparameters; the effective selection thresholds contribute 3), and 66 latent per-star distances. Normal priors are written  $\mathcal{N}(\mu, \sigma)$ ; bounds denote truncation.

map (Green et al. 2019), which covers declinations  $\delta > -30^\circ$ , and the Marshall et al. (2006) map for the inner Galaxy where *Bayestar19* lacks coverage. *Bayestar19* reddening is converted to  $A_H$  using  $R_H = 0.469$  (Green et al. 2019), while Marshall et al. (2006)  $A_{K_s}$  values are converted via  $A_H = 1.55 A_{K_s}$ . The magnitude and parallax likelihoods are Gaussian, centred on the values predicted by the period–luminosity relation and  $1/d - \delta_\varpi$ , respectively; the period and metallicity likelihoods  $\mathcal{L}(\log P_{\text{obs}} | \log P)$  and  $\mathcal{L}([\text{O}/\text{H}]_{\text{obs}} | [\text{O}/\text{H}])$  relate the observed values to the true underlying quantities. The remaining terms are the joint position prior  $\pi(d, \mathbf{\Omega})$  of Eq. (2) and the prior  $\pi(\log P, [\text{O}/\text{H}] | \mathbf{\Lambda})$  on Cepheid properties. In principle, the integral should include both the true sky position  $\mathbf{\Omega}$  and the observed position  $\mathbf{\Omega}_{\text{obs}}$  with the delta-function likelihood of Section 3.3; since this collapses the integral over  $\mathbf{\Omega}_{\text{obs}}$ , we write a single  $\mathbf{\Omega}$  throughout. Assuming that the selection cuts are independent, the joint selection function factorises as

$$S(m, \varpi, \log P_{\text{obs}}, A_H) = S(m) S(\varpi) S(\log P_{\text{obs}}) S(A_H), \quad (29)$$

where each factor takes the  $S_{\text{low}}$  or  $S_{\text{high}}$  form of Eq. (25) depending on whether the cut imposes a lower or upper threshold. This nine-dimensional integral must be evaluated for each observational campaign, but the choice of Gaussian

population priors and likelihoods, combined with modelling the selection cuts as normal CDFs, permits a sequence of analytic marginalisations that reduce it to a tractable form. First, because there is no selection on metallicity and the likelihood is normalised, the integral over  $[\text{O}/\text{H}]_{\text{obs}}$  evaluates to unity and  $[\text{O}/\text{H}]_{\text{obs}}$  drops out. The true metallicity  $[\text{O}/\text{H}]$ , however, remains through the magnitude likelihood. By the same argument as in Eq. (18)—but without the measurement likelihood, equivalent to the  $\epsilon_{[\text{O}/\text{H}]} \rightarrow \infty$  limit of Eq. (19)—the integral over  $[\text{O}/\text{H}]$  evaluates to

$$\int d[\text{O}/\text{H}] \mathcal{L}(m | d, \log P, [\text{O}/\text{H}], \mathbf{\Lambda}) \pi([\text{O}/\text{H}] | \mathbf{\Lambda}) = \mathcal{N}(m | \bar{m}_{\text{pred}}(d, \log P), \sigma_1), \quad (30)$$

where  $\sigma_1^2 = \sigma_m^2 + \sigma_{\text{int}}^2 + Z_W^2 \sigma_{[\text{O}/\text{H}]}^2$  (analogous to  $\sigma_{1,i}$  of Eq. (18) but with  $\sigma_{[\text{O}/\text{H}]}$  replacing  $\tilde{\sigma}_{[\text{O}/\text{H}]}$ , since no per-star measurement enters); here  $\sigma_m$  and  $\sigma_{\text{int}}$  are set to the median values across the campaign rather than per-star quantities—a simplification, since in principle the per-star uncertainties should be sampled within the normalisation integral. The predicted magnitude  $\bar{m}_{\text{pred}}(d, \log P) = M_{H,1}^W + b_W(\log P - 1) + Z_W \mu_{[\text{O}/\text{H}]} + \mu(d)$  is evaluated at the prior mean metallicity  $\mu_{[\text{O}/\text{H}]}$ .

Second, as in the per-star likelihood, the delta-function period likelihood of Eq. (14) collapses the integral over

$\log P_{\text{obs}}$ , setting  $\log P_{\text{obs}} = \log P$  everywhere. By the same argument,  $\bar{m}_{\text{pred}}$  is linear in  $\log P$  through the slope  $b_W$ , so the product of Eq. (30) with the Gaussian period prior is again Gaussian in  $\log P$ . The integral over  $\log P$  with the period selection then yields

$$\begin{aligned} & \int d \log P \mathcal{S}(\log P) \mathcal{N}(m | \bar{m}_{\text{pred}}, \sigma_1) \pi(\log P | \Lambda) \\ &= \mathcal{N}(m | \hat{m}_{\text{pred}}(d), \sigma_2) \\ & \times \Phi \left( \frac{\tilde{\mu}_{\log P}(m, d) - \log P_{\text{min}}}{\sqrt{w_{\log P}^2 + \tilde{\sigma}_{\log P}^2}} \right), \end{aligned} \quad (31)$$

where  $\hat{m}_{\text{pred}}(d) = M_{H,1}^W + b_W(\mu_{\log P} - 1) + Z_W \mu_{[O/H]} + \mu(d)$  is the predicted magnitude at the prior means and  $\sigma_2^2 = \sigma_1^2 + b_W^2 \sigma_{\log P}^2$  the total variance. The quantities  $\tilde{\mu}_{\log P}(m, d)$  and  $\tilde{\sigma}_{\log P}^2$  are the mean and variance of the posterior Gaussian in  $\log P$  obtained from multiplying the magnitude likelihood (which constrains  $\log P$  through the slope  $b_W$ ) with the period prior. Explicitly,

$$\tilde{\sigma}_{\log P}^{-2} = b_W^2 \sigma_1^{-2} + \sigma_{\log P}^{-2}, \quad (32)$$

$$\tilde{\mu}_{\log P}(m, d) = \mu_{\log P} + \frac{b_W \tilde{\sigma}_{\log P}^2}{\sigma_1^2} (m - \hat{m}_{\text{pred}}(d)), \quad (33)$$

analogous to the metallicity expressions of Eq. (19).

After both marginalisations, the detection probability reduces to an integral over  $(\Omega, d)$  and the Gaussian observables  $(m, \varpi)$ . Selection factors that depend deterministically on  $(d, \Omega)$ —such as the extinction cut, evaluated from the three-dimensional dust map—separate from those involving these Gaussian variables. Each remaining selection factor is a smooth threshold on a linear function of the observables: the magnitude and parallax selections act directly on  $m$  and  $\varpi$ , while the period selection inherited from Eq. (31) depends on  $m$  through  $\tilde{\mu}_{\log P}(m, d)$ .

Let  $n$  denote the number of observables with Gaussian likelihoods (among  $m$  and  $\varpi$ ) that enter at least one selection cut. Standardising these into a vector  $\mathbf{z} \in \mathbb{R}^n$ , where each component  $z_i = (x_i - \hat{x}_i)/\sigma_i$  is the standardised residual of the  $i^{\text{th}}$  observable, the product of Gaussian likelihoods becomes  $\phi_n(\mathbf{z})$ , with  $\phi_n$  the  $n$ -variate standard normal density. For example, when both magnitude and parallax selections are applied ( $n = 2$ ),

$$\mathbf{z} = \left( \frac{m - \hat{m}_{\text{pred}}}{\sigma_2}, \frac{\varpi - \varpi_{\text{pred}}}{\sigma_\varpi} \right)^T, \quad (34)$$

where  $\sigma_\varpi$  is set to the median parallax uncertainty of the campaign. Under this substitution, each selection factor takes the form  $\Phi(\alpha_k + \gamma_k^T \mathbf{z})$ , where  $\alpha_k$  is a scalar absorbing the selection threshold and the predicted observable, and  $\gamma_k \in \mathbb{R}^n$  captures the ratio of the likelihood width to the selection width along each observable. Continuing the  $n = 2$  case, an upper magnitude cut and a lower parallax cut yield

$$\begin{aligned} \text{magnitude: } \alpha_1 &= \frac{m_{\text{max}} - \hat{m}_{\text{pred}}}{w_m}, & \gamma_1 &= \left( -\frac{\sigma_2}{w_m}, 0 \right)^T, \\ \text{parallax: } \alpha_2 &= \frac{\varpi_{\text{pred}} - \varpi_{\text{min}}}{w_\varpi}, & \gamma_2 &= \left( 0, \frac{\sigma_\varpi}{w_\varpi} \right)^T, \end{aligned} \quad (35)$$

where each  $\gamma_k$  has a zero entry for the observable that does

not enter that cut. The integral over  $\mathbf{z}$  evaluates analytically:

$$\int d\mathbf{z} \prod_{k=1}^K \Phi(\alpha_k + \gamma_k^T \mathbf{z}) \phi_n(\mathbf{z}) = \Phi_K(\mathbf{h}; \mathbf{R}), \quad (36)$$

where  $\Phi_K$  is the  $K$ -dimensional multivariate normal CDF with zero mean and correlation matrix  $\mathbf{R}$ , and

$$\begin{aligned} h_k &= \frac{\alpha_k}{\sqrt{1 + \|\gamma_k\|^2}}, \\ R_{jk} &= \frac{\gamma_j \cdot \gamma_k}{\sqrt{(1 + \|\gamma_j\|^2)(1 + \|\gamma_k\|^2)}}, \end{aligned} \quad (37)$$

and  $R_{kk} = 1$ . The arguments  $h_k$  absorb the distance-dependent predicted observables and selection thresholds, while  $R_{jk}$  captures correlations between selection criteria that share dependence on the same underlying observables.

Applying this identity, the detection probability collapses to an integral over distance and sky direction only:

$$\begin{aligned} p(S = 1 | \Lambda) &= \int d\Omega dd \mathcal{S}_{\text{ext}}(d, \Omega) \Phi_K(\mathbf{h}(d); \mathbf{R}(d)) \\ & \times \pi(d, \Omega), \end{aligned} \quad (38)$$

where  $\mathcal{S}_{\text{ext}}(d, \Omega) = \Phi((A_{H,\text{max}} - A_H(d, \Omega))/w_{A_H})$  is the extinction selection factor evaluated from the dust map (set to unity when no extinction cut is applied), and  $\Phi_K(\mathbf{h}(d); \mathbf{R}(d))$  encapsulates all  $K$  selection cuts on the Gaussian observables. The dimension  $K$  and the explicit forms of  $\mathbf{h}(d)$  and  $\mathbf{R}(d)$  for each campaign are derived in Sections 3.4.1 and 3.4.2.

Thus, the original nine-dimensional integral of Eq. (28) reduces to a numerical integral over  $(d, \ell, b)$ . The distance integral is evaluated via Simpson's rule on a fine grid for each sightline, while the integral over  $\Omega = (\ell, b)$  is approximated by Monte Carlo sampling. For a uniform-in-volume prior with no extinction cut, the integrand would be independent of  $\Omega$  and the detection probability would reduce to a single one-dimensional integral over  $d$ ; the disk geometry of Eq. (2) and the sightline-dependent extinction, however, require the full angular integration. Expanding  $\pi(d, \Omega) = \varrho(d, \Omega)/\mathcal{Z}_V$  from Eq. (2), where  $\varrho(d, \Omega)$  is the unnormalised disk density of Eq. (16), the factor  $\mathcal{Z}_V^{-1}$  appears identically in the per-star prior and in the detection probability and cancels in the posterior (Section 3.3). Only the unnormalised integral over  $\varrho$  is therefore needed:

$$\begin{aligned} p(S = 1 | \Lambda) & \approx \frac{4\pi}{\mathcal{Z}_V N_{\text{los}}} \sum_{j=1}^{N_{\text{los}}} \int_{d_{\text{min}}}^{d_{\text{max}}} dd \mathcal{S}_{\text{ext}}(d, \Omega_j) \Phi_K(\mathbf{h}(d); \mathbf{R}(d)) \\ & \times \varrho(d, \Omega_j), \end{aligned} \quad (39)$$

where the  $\Omega_j$  are sampled uniformly on the sky and the distance integral along each sightline is evaluated via Simpson's rule on a fine grid. In practice, we importance-sample the  $\Omega_j$  from  $\pi(\Omega)$  (Eq. 5) to concentrate draws near the Galactic plane, where  $\varrho$  is largest.

#### 3.4.1 C27 selection

The C27 sample targets nearby Cepheids, selected primarily on the photometry-predicted parallax  $\varpi_{\text{pred}} > 0.8$  mas computed following Eq. (1). Because this selection was applied

using a fixed set of fiducial period–luminosity parameters, modelling the criterion exactly would couple the selection function to those assumed values. We instead approximate this as a smooth lower cut on the observed parallax at  $\varpi_{\min}$  with a transition width  $w_{\varpi} = 0.05$  mas, which is independent of  $\mathbf{\Lambda}$ . We similarly assume a lower cut on the Wesenheit magnitude at  $m_{H,\min}^W$  to exclude the nearest, brightest Cepheids. The effective threshold  $m_{H,\min}^W$  is inferred with a uniform prior. Although C27 also applied an extinction cut ( $A_H < 0.6$  mag), we treat this as negligible for the nearby C27 sample. The per-star selection weight is therefore

$$\mathcal{S}(\mathbf{x}_{\text{obs},i}) = \Phi\left(\frac{\varpi_{\text{obs},i} - \varpi_{\min}}{w_{\varpi}}\right) \Phi\left(\frac{m_{H,\text{obs},i}^W - m_{H,\min}^W}{w_m}\right), \quad (40)$$

depending only on the observed parallax and magnitude.

For the marginalised detection probability, the [O/H] and  $\log P$  integrals proceed as in Eqs. (30) and (31), but without a period selection cut; the  $\log P$  marginalisation therefore yields a Gaussian in  $m$  with variance  $\sigma_2^2$  and mean  $\hat{m}_{\text{pred}}(d)$ , without the  $\Phi$  factor of Eq. (31). The two remaining selection factors act on separate Gaussian observables ( $K = 2$ ,  $n = 2$ ): the magnitude cut on  $m$  and the parallax cut on  $\varpi$ . Since these are independent given the distance, the correlation matrix  $\mathbf{R}$  is diagonal and  $\Phi_2(\mathbf{h}; \mathbf{R})$  factorises as  $\Phi(h_1)\Phi(h_2)$ . Setting  $\mathcal{S}_{\text{ext}} = 1$  in Eq. (38), the C27 detection probability is

$$p(S = 1 | \mathbf{\Lambda}) = \int d\mathbf{\Omega} dd \Phi(h_1(d)) \Phi(h_2(d)) \times \pi(d, \mathbf{\Omega}), \quad (41)$$

where

$$h_1(d) = \frac{\hat{m}_{\text{pred}}(d) - m_{H,\min}^W}{\sqrt{w_m^2 + \sigma_2^2}}, \quad h_2(d) = \frac{\varpi_{\text{pred}}(d) - \varpi_{\min}}{\sqrt{w_{\varpi}^2 + \sigma_{\varpi}^2}}. \quad (42)$$

Following Eq. (39), we evaluate Eq. (41) with  $\mathcal{S}_{\text{ext}} = 1$ ,  $N_{\text{los}} = 5000$  sightlines,  $d_{\min} = 0.1$  kpc, and  $d_{\max} = 2.0$  kpc. Because the analytic marginalisation reduces the problem to a set of one-dimensional integrals over distance, the detection probability is computationally tractable even on-the-fly during sampling.

### 3.4.2 C22 selection

The C22 sample is subject to four selection criteria. The original photometric selection was not performed in the Wesenheit band; however, we approximate it as an effective upper cut on the Wesenheit magnitude,  $m_H^W < m_{H,\max}^W$ , noting that the magnitude threshold is sufficiently broad that the sensitivity to the choice of band is minimised. We similarly model an effective lower cut on the observed parallax,  $\varpi_{\text{obs}} > \varpi_{\min}$ , and a lower cut on pulsation period,  $\log P > \log P_{\min}$ ; an extinction cut,  $A_H < A_{H,\max}$ , is optionally included but disabled in the fiducial model (Section 5.4). The effective thresholds  $\varpi_{\min}$  and  $m_{H,\max}^W$  are jointly in-

ferred with uniform priors. The per-star selection weight is

$$\mathcal{S}(\mathbf{x}_{\text{obs},i}, d_i) = \Phi\left(\frac{m_{H,\max}^W - m_{H,\text{obs},i}^W}{w_m}\right) \Phi\left(\frac{\varpi_{\text{obs},i} - \varpi_{\min}}{w_{\varpi}}\right) \times \Phi\left(\frac{\log P_{\text{obs},i} - \log P_{\min}}{w_{\log P}}\right) \times \Phi\left(\frac{A_{H,\max} - A_H(d_i, \ell_i, b_i)}{w_{A_H}}\right), \quad (43)$$

where the extinction factor depends on the latent distance  $d_i$  through the three-dimensional dust map.

The marginalised detection probability follows Eq. (39). The period selection enters through the  $\Phi$  factor of Eq. (31), which depends on  $m$  via  $\hat{\mu}_{\log P}(m, d)$ . Combined with the magnitude cut, this gives  $K = 3$  selection factors acting on  $n = 2$  Gaussian observables ( $m$  and  $\varpi$ ):

$$h_1(d) = \frac{m_{H,\max}^W - \hat{m}_{\text{pred}}(d)}{\sqrt{w_m^2 + \sigma_2^2}}, \quad h_2(d) = \frac{\varpi_{\text{pred}}(d) - \varpi_{\min}}{\sqrt{w_{\varpi}^2 + \sigma_{\varpi}^2}}, \quad h_3 = \frac{\mu_{\log P} - \log P_{\min}}{\sqrt{w_{\log P}^2 + \sigma_{\log P}^2}}. \quad (44)$$

Because the parallax cut depends only on  $\varpi$  while the magnitude and period cuts depend only on  $m$ , the correlation matrix has  $R_{12} = R_{23} = 0$  and a single non-zero off-diagonal entry

$$R_{13} = \frac{-b_W \sigma_{\log P}^2}{\sqrt{(w_m^2 + \sigma_2^2)(w_{\log P}^2 + \sigma_{\log P}^2)}}, \quad (45)$$

which is positive (since  $b_W < 0$ ) and captures the correlation between the magnitude and period cuts through their shared dependence on the latent period. The trivariate CDF therefore factorises as  $\Phi_3(\mathbf{h}; \mathbf{R}) = \Phi(h_2)\Phi_2(h_1, h_3; R_{13})$ . The bivariate CDF is evaluated via the integral representation

$$\Phi_2(x_1, x_2; \rho) = \Phi(x_1)\Phi(x_2) + \int_0^\rho \phi_2(x_1, x_2; t) dt, \quad (46)$$

where  $\phi_2(x_1, x_2; t)$  is the standard bivariate normal density with correlation  $t$ . The integrand is smooth and the integral is computed to high accuracy with a low-order Gauss–Legendre quadrature rule, making the evaluation of  $\Phi_2$  essentially as fast as that of the univariate  $\Phi$ . When the extinction cut is enabled, the extinction selection  $\mathcal{S}_{\text{ext}}(d, \mathbf{\Omega}) = \Phi((A_{H,\max} - A_H(d, \mathbf{\Omega}))/w_{A_H})$  is included in the integrand; in the fiducial model  $\mathcal{S}_{\text{ext}} = 1$ . We use  $N_{\text{los}} = 5000$  sightlines,  $d_{\min} = 0.1$  kpc, and  $d_{\max} = 8.5$  kpc.

### 3.4.3 LMC and N4258 selection

The period truncation at  $\log P_{\text{cut}} = -0.3$  common to both the LMC and N4258 catalogues is accounted for as described in Section 3.3 (Eq. 24). Beyond this, we do not model further selection effects for the LMC and N4258 Cepheids. A complete treatment would additionally address magnitude-dependent selection within each galaxy. For the LMC ( $\mu \approx 18.5$ ), Cepheids at the period cut have  $m_H^W \approx 17$  mag, far brighter than any *HST* detection limit; magnitude selection is therefore irrelevant. For N4258 ( $\mu \approx 29.4$ ), the faintest

Cepheids reach  $m_H^W \approx 28$  mag, still brighter than but approaching the *HST* WFC3/IR detection limit in crowded fields. Modelling this would require integrating the multivariate likelihood of Eq. (23) over the selection region and marginalising over the magnitudes of undetected Cepheids, whose covariance with the observed sample is not available.

### 3.5 Full posterior and inference

Combining the priors, likelihoods, and selection modelling, the full posterior is

$$\begin{aligned} \mathcal{P}(\mathbf{A}, \{d_i\}, \{d_j\} \mid \mathbf{D}) &\propto \pi(\mathbf{A}) \\ &\times \prod_{p \in \{C22, C27\}} \left[ [p_p(S = 1 \mid \mathbf{A})]^{-n_p} \right. \\ &\times \left. \prod_{i \in p} \mathcal{L}_i \mathcal{S}(\mathbf{x}_{\text{obs},i}, d_i) \pi(d_i, \ell_i, b_i) \right] \\ &\times \prod_{j \in \{LMC, N4258\}} [p_j(S = 1 \mid \mathbf{A})]^{-N_j} \mathcal{L}_j^{\text{marg}} \mathcal{L}(\tilde{\mu}_j \mid \mu_j) \pi(d_j). \end{aligned} \quad (47)$$

The first product runs over the MW campaigns, where  $n_p$  is the number of Cepheids in campaign  $p$ ,  $\mathcal{L}_i$  the marginalised per-star likelihood of Eq. (20),  $\mathcal{S}(\cdot)$  the per-star selection weight of Eqs. (40) and (43),  $p_p(S = 1 \mid \mathbf{A})$  the campaign-level detection probability of Eq. (28), and  $\pi(d_i, \ell_i, b_i)$  the joint position prior of Eq. (2). The second product runs over the LMC and N4258, where  $p_j(S = 1 \mid \mathbf{A})$  is the per-star period detection probability of Eq. (24),  $\mathcal{L}_j^{\text{marg}}$  the marginalised host Cepheid likelihood of Eq. (23),  $\mathcal{L}(\tilde{\mu}_j \mid \mu_j)$  the geometric distance constraint of Eq. (21), and  $\pi(d_j)$  a uniform-in-volume distance prior. All Cepheids within a given host galaxy are placed at a common distance  $d_j$ , which is a free parameter of the model.

The sampled parameters are therefore the global parameters  $\mathbf{A}$ —comprising the shared period–luminosity relation parameters, the parallax offset, the per-campaign intrinsic scatters, and the population hyperparameters—together with the distance  $d_i$  to each MW Cepheid and the distance  $d_j$  to each host galaxy. Table 1 lists the observables entering the model, and Table 3 collects all inferred and fixed parameters alongside the populations to which they apply; in total the model has 91 sampled parameters. We implement the model in JAX and sample with the No-U-Turn Sampler (NUTS; Hoffman & Gelman 2011) via `numpyro`<sup>2</sup> (Phan et al. 2019). We run four independent chains, each with 1000 warm-up and 5000 sampling steps, and verify convergence by requiring  $\hat{R} < 1.01$  for all parameters; we collect at least 5000 effective samples per parameter.

For comparison, we also implement the R21 parallax-space model, which avoids sampling per-star distances. For each Cepheid, we compute a photometric parallax from the observed Wesenheit magnitude and the period–luminosity relation,

$$\varpi_{\text{phot}} = 10^{-0.2(m_H^W - M_{H,\text{pred}}^W - 10)}, \quad (48)$$

and the  $\chi^2$  per star is

$$\chi_i^2 = \frac{(\varpi_{\text{obs}} - \varpi_{\text{phot}} + \delta_\varpi)^2}{\tilde{\sigma}_{\varpi,i}^2}, \quad (49)$$

where

$$\tilde{\sigma}_{\varpi,i}^2 = (0.2 \ln 10 \varpi_{\text{phot}} \sigma_{m,\text{tot}})^2 + (\alpha \sigma_{\varpi,\text{EDR3}})^2 \quad (50)$$

combining the propagated magnitude uncertainty with the *Gaia* parallax error inflated by a factor  $\alpha = 1.1$ . This model applies no additional selection modelling and fixes the intrinsic scatter to 0.06 mag<sup>3</sup>.

## 4 RESULTS

The fiducial inference combines the C22 and C27 samples with the disk distance prior (Eq. 2) and selection modelling applied to both MW campaigns; the LMC and N4258 are optionally included as additional geometric calibrators. The term ‘‘MW Cepheids’’ denotes the joint C22 + C27 sample; individual campaign results appear in Appendix B. Subsequent variants omit the selection modelling or replace the disk prior with a uniform-in-volume prior.

The R21  $\chi^2$  method applied to the MW Cepheids yields results closely matching our forward model. In Appendix D we show that this agreement is driven by the small intrinsic scatter of the period–luminosity relation, and in Appendix E we validate the inference methods on mock catalogues mimicking the C22 and C27 campaigns.

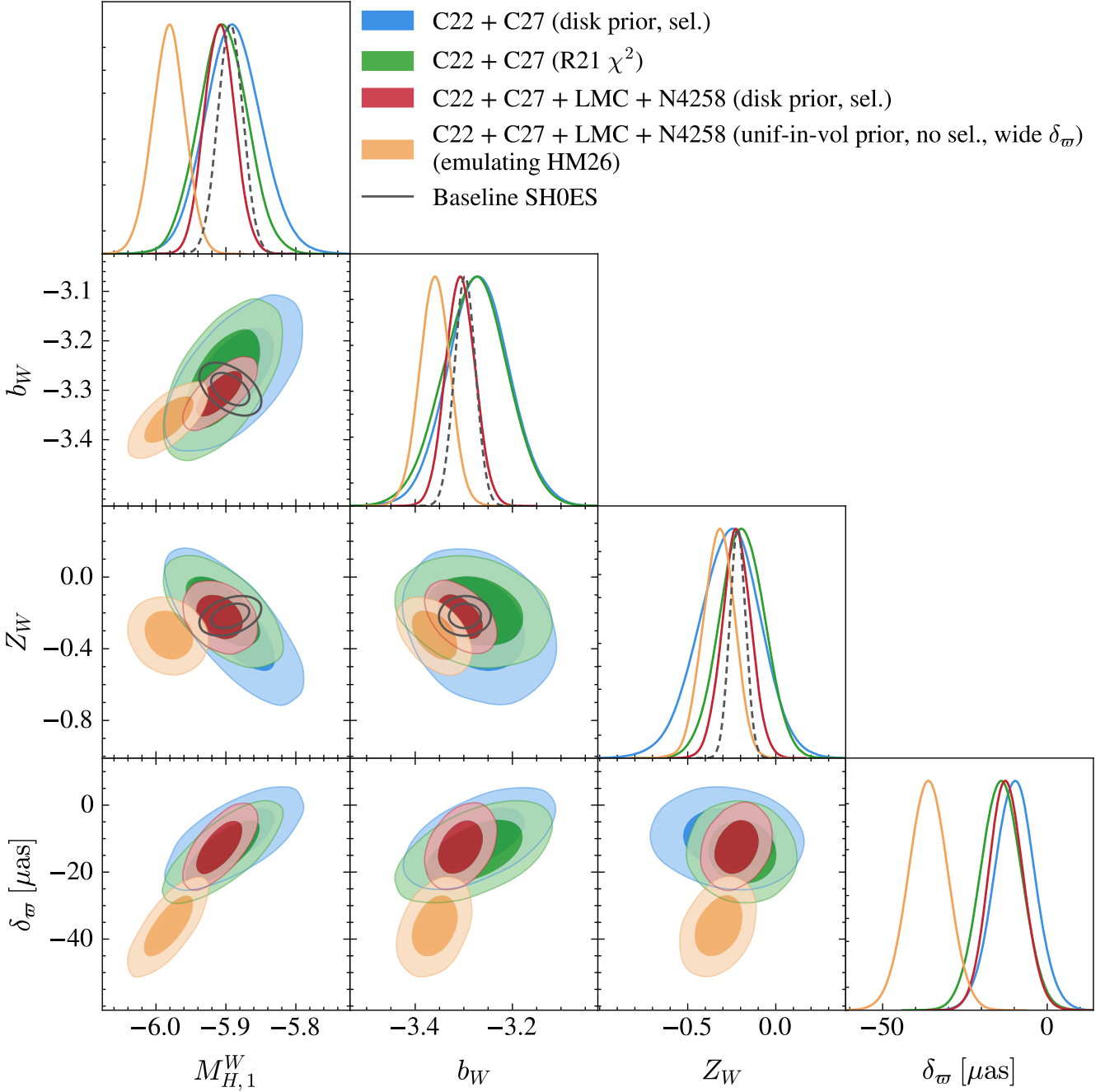
### 4.1 Fiducial posteriors

Figure 4 shows the marginalised posterior of the period–luminosity parameters ( $M_{H,1}^W, b_W, Z_W$ ) and the parallax offset  $\delta_\varpi$  for three model configurations: (i) C22 and C27 with the disk prior and selection modelling but without the LMC and N4258, (ii) the same with the LMC and N4258 Cepheid populations and their geometric distance calibrations, and (iii) a model including all four populations that neglects selection modelling, adopts a uniform-in-volume MW distance prior, and uses a wide  $\delta_\varpi$  prior, designed to emulate the analysis of HM26.

The MW-only posterior is substantially wider, by factors of 1.8, 2.1, and 2.1 in  $M_{H,1}^W, b_W$ , and  $Z_W$ , respectively, but only by a factor of 1.2 in  $\delta_\varpi$ . Both  $b_W$  and  $Z_W$  are strongly correlated with  $M_{H,1}^W$  in the MW-only inference; including the LMC and N4258 Cepheids breaks these degeneracies. Since  $\delta_\varpi$  enters only through the MW parallaxes, the LMC and N4258 do not substantially tighten the constraint; the fiducial posterior gives  $\delta_\varpi = -12.4 \pm 5.3 \mu\text{as}$ , compared with  $-9.9 \pm 6.1 \mu\text{as}$  from the MW-only inference. For comparison, Cruz Reyes & Anderson (2023) report  $\delta_\varpi = -19 \pm 3 \mu\text{as}$  from *Gaia* DR3 parallaxes of open clusters hosting Cepheids; the difference reflects the sensitivity of the inferred offset to the assumed prior and sample composition. The addition of the LMC and N4258 introduces no tension

<sup>3</sup> We note that R21 unintentionally fixed the parameters in the  $\varpi_{\text{phot}}$  expression (Eq. (48)) when computing the error terms (Eq. (50)), but we allow them to vary here, which may contribute to the  $\sim 0.01$  mag difference between R21 as reported and our emulation as shown in Table 4.

<sup>2</sup> `num.pyro.ai`



**Figure 4.** Marginalised posterior of the period–luminosity parameters ( $M_{H,1}^W$ ,  $b_W$ ,  $Z_W$ ) and the parallax offset  $\delta_\pi$  for three model configurations: C22 and C27 (MW only) with a MW disk distance prior and selection (blue, filled), the fiducial model including the LMC and N4258 with the same MW disk prior and selection (red, filled), and all four populations with a uniform-in-volume MW distance prior, no selection, and a wide  $\delta_\pi$  prior, emulating **HM26** (orange). The  $0.7\sigma$  agreement in  $M_{H,1}^W$  with the baseline SH0ES value translates to a shift in  $H_0$  of less than  $0.2 \text{ km s}^{-1} \text{ Mpc}^{-1}$  (Section 5.3). The baseline SH0ES contours from **R22** are shown in black, and the **R21**  $\chi^2$  contours for C22 + C27 are shown in green. The baseline SH0ES (**R22**) constraints derive from the full three-rung fit (geometric anchors, Cepheids, and Type Ia supernovae), while the **R21**  $\chi^2$  uses only the MW Cepheid parallaxes. For visual clarity, the SH0ES constraints are dashed in the panels along the diagonal. All contours show the  $1\sigma$  and  $2\sigma$  credible regions.

with the MW-only result. We also compare these posteriors to the baseline SH0ES contours from the joint three-rung fit reported in table 5 of **R22**, combining geometric calibrators, MW and extragalactic Cepheids, and Type Ia supernovae. All three parameters agree with our fiducial posteriors to within  $1\sigma$ .

Applying the **R21**  $\chi^2$  method to the C22 and C27 samples yields  $M_{H,1}^W = -5.904 \pm 0.035 \text{ mag}$  and  $\delta_\pi = -14.0 \pm 6.3 \mu\text{as}$  (Table 4). Compared to our MW-only forward model with selection ( $M_{H,1}^W = -5.889 \pm 0.040 \text{ mag}$ ,  $\delta_\pi = -9.9 \pm 6.1 \mu\text{as}$ ), the  $\chi^2$  method recovers a  $\sim 0.02 \text{ mag}$  brighter zero-point and a  $\sim 4 \mu\text{as}$  more negative parallax offset. On the

other hand, our MW-only forward model zero-point more closely agrees with the  $M_{H,1}^W = -5.903 \pm 0.024$  mag reported in table 4 of R22 from a global period–luminosity fit to the R21 sample, differing by  $0.4\sigma$ . It likewise agrees with the baseline SH0ES value of  $M_{H,1}^W = -5.894$  mag (table 2 of R22) to within  $0.1\sigma$ . Including the LMC and N4258 tightens the constraint and brings the zero-point into closer agreement: the fiducial  $M_{H,1}^W = -5.909 \pm 0.022$  mag differs from the R22 table 4 value by  $0.006$  mag ( $0.3\sigma$ ) and from the baseline SH0ES value by  $0.7\sigma$ . This  $0.7\sigma$  shift corresponds to a change in  $H_0$  of less than  $0.2 \text{ km s}^{-1} \text{ Mpc}^{-1}$ ; the implications are further discussed in Section 5.3.

Figure 5 shows the marginalised posterior distributions of the per-campaign intrinsic scatter  $\sigma_{\text{int}}$ . The C22 scatter peaks at  $\sim 0.07$  mag, roughly 1.8 times larger than the C27 value of  $\sim 0.04$  mag, possibly reflecting residual extinction scatter in the more distant C22 sample, where dust corrections are larger and the Wesenheit magnitude does not fully remove sightline-to-sightline variations in the reddening law. Including the LMC and N4258 tightens the period–luminosity relation parameters but leaves the MW scatter posteriors unchanged, as expected since  $\sigma_{\text{int}}$  is determined by the spread of MW magnitudes about the relation and is largely independent of the global zero-point.

To test whether the MW, LMC, and N4258 scatters are consistent, we run two additional configurations. First, we impose a single shared  $\sigma_{\text{int}}$  across all four populations (with the  $0.06$  mag already in  $\Sigma_j$  subtracted in quadrature for the LMC and N4258). The  $\sim 500$  LMC and N4258 Cepheids dominate the constraint, yielding  $\sigma_{\text{int}} = 0.063 \pm 0.009$  mag; without these populations the same shared model gives  $\sigma_{\text{int}} = 0.051 \pm 0.015$  mag, a  $1.7\times$  wider uncertainty. Second, we allow separate scatters for C22, C27, and the LMC + N4258 jointly. The LMC + N4258 scatter is  $\sigma_{\text{int}}^{\text{LMC+N4258}} = 0.070 \pm 0.010$  mag, roughly 15% larger than the  $0.06$  mag assumed by R22, while the MW campaigns separate cleanly:  $\sigma_{\text{int}}^{\text{C22}} = 0.071 \pm 0.022$  mag and  $\sigma_{\text{int}}^{\text{C27}} = 0.041 \pm 0.015$  mag. Despite these differences, the period–luminosity parameters are robust to the scatter model:  $M_{H,1}^W$ ,  $b_W$ , and  $Z_W$  shift by less than  $0.3\sigma$  between the shared and per-campaign configurations when the LMC and N4258 are included. We also run models with a free parallax uncertainty scaling  $f_\varpi$  that multiplies the reported *Gaia* parallax uncertainties (R21 adopt a fixed factor of 1.1). With a single shared  $\sigma_{\text{int}}$  across C22 and C27 in the MW-only configuration, we obtain  $\sigma_{\text{int}} = 0.039 \pm 0.016$  mag,  $f_\varpi = 1.23 \pm 0.16$ , and  $\delta_\varpi = -8.5 \pm 6.4 \mu\text{as}$  (Table 4). The inferred  $f_\varpi > 1$  indicates that the reported parallax uncertainties may be mildly underestimated. Analysing each campaign separately with the LMC and N4258, we find  $f_\varpi = 1.24 \pm 0.18$  for C22 and  $f_\varpi = 0.71 \pm 0.33$  for C27. In all cases,  $f_\varpi$  has negligible impact on the inferred period–luminosity parameters and parallax offset.

The fiducial result is robust to the choice of  $\delta_\varpi$  prior: switching to a uniform prior shifts  $\delta_\varpi$  by  $4.8 \mu\text{as}$  (from  $-12.4$  to  $-17.2 \mu\text{as}$ ) while  $M_{H,1}^W$  changes by  $0.013$  mag, both well within the posterior uncertainties. Similarly, replacing the axisymmetric disk prior with the spiral-arm-modulated prior of Appendix A leaves the posteriors unchanged:  $\delta_\varpi$  shifts by  $0.4 \mu\text{as}$  and  $M_{H,1}^W$  by  $0.001$  mag. Posterior means and standard deviations for all model variants are reported in Table 4.

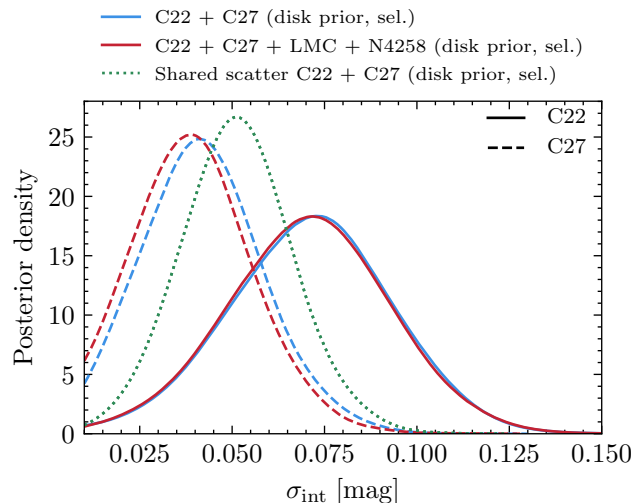


**Figure 5.** Marginalised posterior of the intrinsic scatter  $\sigma_{\text{int}}$  for C22 (solid) and C27 (dashed), comparing the MW-only model with separate per-campaign scatters (blue), the fiducial model including the LMC and N4258 with separate scatters (red), and the MW-only model with a single shared  $\sigma_{\text{int}}$  for both campaigns (green dotted;  $0.051 \pm 0.015$  mag). Including the LMC and N4258 and inferring their joint scatter yields  $\sigma_{\text{int}} = 0.063 \pm 0.009$  mag.

## 4.2 Impact of selection modelling and distance prior

To quantify the impact of selection modelling and the distance prior, we replace the disk prior with a uniform-in-volume prior for the MW Cepheids (retaining only the aforementioned per-campaign  $d_{\text{min}}$  and  $d_{\text{max}}$  for normalisation) and disable the selection modelling. The resulting posteriors are incompatible with the fiducial model:  $M_{H,1}^W$  shifts to brighter values by  $\sim 0.05$  mag and  $\delta_\varpi$  to more negative values by  $\sim 14 \mu\text{as}$ .

Table 4 reports further model variants that isolate the individual contributions of the selection modelling and distance prior. Disabling the selection modelling alone (disk prior, no selection) in the C22 + C27 + LMC + N4258 configuration shifts  $\delta_\varpi$  from  $-12.4$  to  $-22.3 \mu\text{as}$  and  $M_{H,1}^W$  from  $-5.909$  to  $-5.938$  mag; additionally replacing the disk prior with a uniform-in-volume prior moves  $\delta_\varpi$  to  $-26.4 \mu\text{as}$  and  $M_{H,1}^W$  to  $-5.954$  mag. The selection modelling and the disk prior therefore act in the same direction, each pulling  $\delta_\varpi$  toward zero and  $M_{H,1}^W$  toward fainter values. Their contributions differ substantially, however. Replacing the disk prior with a uniform-in-volume prior while retaining the selection modelling shifts  $M_{H,1}^W$  by only  $0.002$  mag and  $\delta_\varpi$  by  $0.2 \mu\text{as}$ , well within the posterior uncertainties. Selection modelling alone accounts for  $\sim 0.03$  mag in  $M_{H,1}^W$  and  $\sim 10 \mu\text{as}$  in  $\delta_\varpi$ , substantially larger than the prior effect. Once the selection function is correctly modelled, the shape of the distance prior—disk or uniform-in-volume—is effectively irrelevant: the per-star likelihood constrains each distance to a narrow interval over which the disk geometry varies minimally. Without the LMC and N4258, the shifts are larger still: the MW-only inference without selection yields  $\delta_\varpi = -23.6 \pm 6.0 \mu\text{as}$  and  $M_{H,1}^W = -5.950 \pm 0.039$  mag with the disk prior, and  $\delta_\varpi = -30.1 \pm 6.2 \mu\text{as}$  and  $M_{H,1}^W = -5.984 \pm 0.039$  mag with the uniform-in-volume prior. These

Model	$M_{H,1}^W$	$b_W$	$Z_W$	$\delta_\varpi$ [ $\mu\text{as}$ ]	$\sigma_{\text{int}}^{\text{C22}}$	$\sigma_{\text{int}}^{\text{C27}}$
Bayesian forward model: <b>disk prior + selection modelling</b>						
<b>Baseline: C22 + C27 + LMC + N4258</b>	<b><math>-5.909 \pm 0.022</math></b>	<b><math>-3.307 \pm 0.030</math></b>	<b><math>-0.22 \pm 0.08</math></b>	<b><math>-12.4 \pm 5.3</math></b>	<b><math>0.071 \pm 0.022</math></b>	<b><math>0.040 \pm 0.016</math></b>
C22 + C27	$-5.889 \pm 0.040$	$-3.269 \pm 0.064$	$-0.27 \pm 0.18$	$-9.9 \pm 6.1$	$0.071 \pm 0.022$	$0.043 \pm 0.016$
C22 + C27 + LMC + N4258 (spiral arms)	$-5.910 \pm 0.022$	$-3.307 \pm 0.030$	$-0.23 \pm 0.08$	$-12.8 \pm 5.3$	$0.070 \pm 0.022$	$0.040 \pm 0.015$
C22 + C27 (shared $\sigma_{\text{int}}$ , free $f_\varpi$ )	$-5.888 \pm 0.039$	$-3.262 \pm 0.064$	$-0.24 \pm 0.18$	$-8.5 \pm 6.4$	$0.039 \pm 0.016$	
C22 + C27 + LMC + N4258 (wide $\delta_\varpi$ prior)	$-5.922 \pm 0.023$	$-3.315 \pm 0.031$	$-0.24 \pm 0.08$	$-17.2 \pm 6.0$	$0.068 \pm 0.022$	$0.040 \pm 0.015$
Bayesian forward model: <b>uniform-in-volume vs. disk prior + no selection modelling</b> ( <i>misspecified</i> ; for comparison with HM26)						
HM26 as reported	<b><math>-5.959 \pm 0.018</math></b>	—	—	<b><math>-26.2 \pm 5.0</math></b>	—	—
C22 + C27 + LMC + N4258 (emulating HM26: uniform-in-volume, wide $\delta_\varpi$ )	$-5.982 \pm 0.023$	$-3.360 \pm 0.031$	$-0.33 \pm 0.09$	$-36.3 \pm 6.1$	$0.075 \pm 0.022$	$0.041 \pm 0.015$
C22 + C27 + LMC + N4258 (uniform-in-volume)	$-5.954 \pm 0.021$	$-3.341 \pm 0.030$	$-0.28 \pm 0.08$	$-26.4 \pm 5.1$	$0.070 \pm 0.021$	$0.039 \pm 0.015$
C22 + C27 (uniform-in-volume)	$-5.984 \pm 0.039$	$-3.408 \pm 0.065$	$-0.22 \pm 0.17$	$-30.1 \pm 6.2$	$0.075 \pm 0.021$	$0.037 \pm 0.015$
C22 + C27 + LMC + N4258 (disk prior)	$-5.938 \pm 0.021$	$-3.328 \pm 0.030$	$-0.26 \pm 0.08$	$-22.3 \pm 5.0$	$0.068 \pm 0.021$	$0.039 \pm 0.015$
C22 + C27 (disk prior)	$-5.950 \pm 0.039$	$-3.353 \pm 0.063$	$-0.23 \pm 0.17$	$-23.6 \pm 6.0$	$0.070 \pm 0.021$	$0.039 \pm 0.015$
Frequentist $\chi^2$ (method used in R21)						
R21 as reported (C22 + C27)	<b><math>-5.915 \pm 0.030</math></b>	$-3.28 \pm 0.06$	$-0.20 \pm 0.13$	$-14.0 \pm 6$	0.06 (fixed)	0.06 (fixed)
R22 reported baseline (C22 + C27 + LMC + N4258)	$-5.894 \pm 0.017$	$-3.299 \pm 0.015$	$-0.217 \pm 0.046$	—	0.06 (fixed)	0.06 (fixed)
R21 $\chi^2$ emulation (C22 + C27)	$-5.904^a \pm 0.035$	$-3.277 \pm 0.066$	$-0.19 \pm 0.13$	$-14.0 \pm 6.3$	—	—
R21 $\chi^2$ emulation (C22 + C27 + LMC + N4258)	$-5.911 \pm 0.022$	$-3.309 \pm 0.030$	$-0.19 \pm 0.08$	$-15.3 \pm 5.3$	—	—

**Table 4.** Posterior means and standard deviations for several model variants. The fiducial configuration is shown in bold. A “+” denotes a joint inference in which the campaigns share period–luminosity parameters but retain separate selection functions and population hyperpriors. Parenthetical labels indicate departures from this baseline (distance prior or  $\delta_\varpi$  prior width). “Wide  $\delta_\varpi$ ” replaces the fiducial  $\mathcal{N}(0, 10)$   $\mu\text{as}$  prior with a uniform prior over  $[-100, 100]$   $\mu\text{as}$ . Variants without selection modelling are ordered from the most biased (closest to HM26) to the least. The frequentist  $\chi^2$  section is shown for comparison with R21 and R22. The spiral arm modulation of the distance prior is described in Appendix A. <sup>a</sup> The difference between R21 as reported and our emulation for C22 + C27 is the result of R21 fixing the period–luminosity parameters where they appear in the error terms.

models neglect the known selection criteria and therefore yield biased posteriors; they are reported to quantify the magnitude of the bias, not as reliable inferences.

### 4.3 Model validation

To verify that the forward model reproduces the observed data, we perform a posterior predictive check (PPC), shown in Fig. 6. For each of 1000 thinned posterior draws, we generate mock MW Cepheids by sampling distances from the disk prior and periods and metallicities from the inferred population distributions, then computing apparent magnitudes and parallaxes from the period–luminosity relation and parallax offset. Observational noise is bootstrapped from the data, and each mock candidate is accepted only if it passes the probabilistic selection function. The resulting distributions of  $m_H^W$ ,  $\varpi$ , and  $\log P$  closely match the observed data, with two-sample Kolmogorov–Smirnov  $p$ -values of 0.33, 0.22, and 0.99, respectively. The joint  $\varpi_{\text{obs}} - m_H^W$  distribution (Fig. 6, bottom right) confirms that the forward model also reproduces the observed correlation between parallax and magnitude. Even when analysing the C22 or C27 samples individually, the forward model with selection reproduces the observed distributions for each campaign. To illustrate the bias introduced by neglecting the selection function and adopting a uniform-in-volume prior for the MW Cepheids, Fig. 6

also shows the corresponding PPC. This model predicts systematically fainter magnitudes and smaller parallaxes than observed and is clearly incompatible with the data. The predicted parallax distribution is bimodal, reflecting the two observational campaigns; a single shared distance range would exacerbate the discrepancy further.

In Appendix C, we compare the per-star distance moduli inferred from the forward model with photometric predictions from the baseline SH0ES period–luminosity parameters; the residuals scatter about zero with no significant systematic offset.

## 5 DISCUSSION

### 5.1 Comparison with previous approaches

We present a forward-modelling framework for the MW, LMC, and N4258 Cepheid samples that incorporates physically motivated priors—including the thin-disk geometry of the MW—and includes a rigorous treatment of the sample selection function, the neglect of which otherwise biases the inference. Stiskalek et al. (2026) introduced a related framework for extragalactic Cepheids, inferring  $H_0$  without supernovae but compressing the MW calibration into a single Gaussian constraint on  $M_{H,1}^W$ . Here we model the MW sample star by star, lifting that compression.

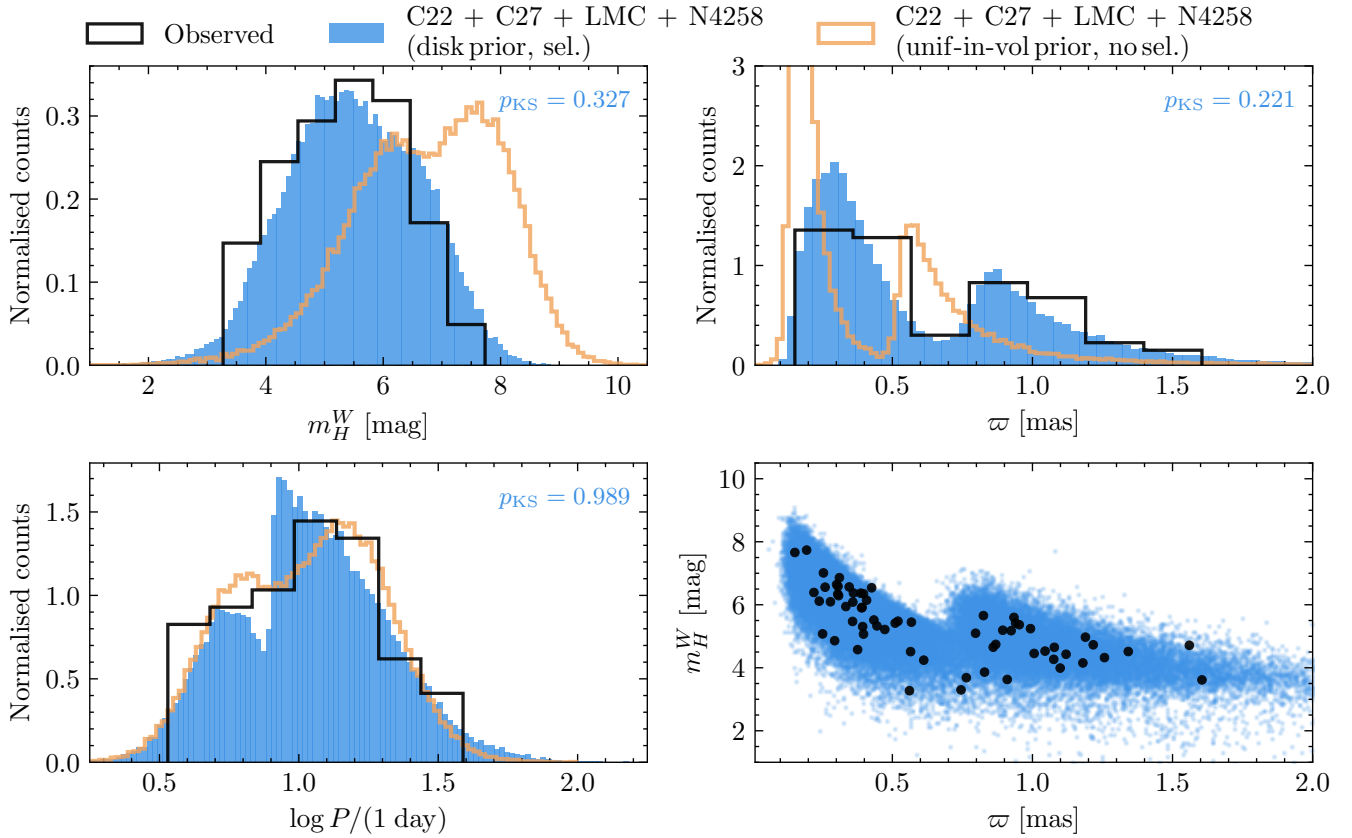


**Figure 6.** PPCs for two model variants: the fiducial model (C22 + C27 + LMC + N4258, disk prior, with selection) and the model with a uniform-in-volume prior and no selection, emulating HM26. Marginal panels compare normalised histograms of the observed (black) and simulated  $m_H^W$ ,  $\varpi$ , and  $\log P$ , each annotated with the two-sample KS  $p$ -value for the fiducial model (which is effectively zero for the model without selection); the bottom-right panel shows the joint  $\varpi$ – $m_H^W$  distribution for the fiducial model. The effective selection thresholds are inferred jointly with the period–luminosity parameters (Table 3), except for the C27 parallax cut which is fixed.

The standard treatment, such as that of Riess et al. (2016) or R21, minimises a  $\chi^2$  between observed parallaxes and the photometric predictions of the period–luminosity relation, with no explicit priors or selection modelling. On the Bayesian side, several efforts have tackled the problem. Cardona et al. (2017) marginalise over hyperparameters that scale the per-star uncertainties, effectively down-weighting outliers. Delgado et al. (2019) construct a hierarchical Bayesian model for period–luminosity relations from *Gaia* parallaxes, placing a joint Gaussian-mixture hyperprior on period, metallicity, and parallax to capture their correlations. Feeney et al. (2018) build a hierarchical model of the full distance ladder—from MW Cepheids through extragalactic Cepheids to Hubble-flow supernovae—inferring  $H_0$  end to end.

What all three Bayesian approaches share is the absence of a principled treatment of the selection function. Delgado et al. (2019) implicitly learn the correlation structure of period, metallicity, and parallax through their Gaussian-mixture hyperprior, which acts as a proxy for selection modelling: it allows the model to discover that longer-period Cepheids are brighter and therefore observed at larger distances (smaller parallaxes in their parametrisation). In reality, this correlation is induced by selection without being present in the intrinsic population; it ought therefore to be

captured by an explicit selection treatment, as we construct here.

Feeney et al. (2018), by contrast, adopt a uniform prior on the distance modulus, which does not reflect the (approximately) uniform-in-volume distribution of extragalactic objects. At small redshifts, a uniform-in-distance-modulus prior goes as  $1/d$ , favouring closer objects, whereas a uniform-in-volume prior goes as  $d^2$ , favouring more distant ones. The similarity between results using a uniform-in-distance-modulus prior and those from a uniform-in-volume prior with selection modelling in this case is not coincidental. In Appendix D we show that, for the MW Cepheid calibration specifically, the per-star forward-model likelihood is well approximated by the R21  $\chi^2$  after marginalising over the latent distance and linearising the distance modulus. This relies on the very small intrinsic scatter of the Cepheid period–luminosity relation,  $\sim 0.05$  mag (here) or 2–3% in distance; it has not been demonstrated to hold even approximately in other settings, where larger intrinsic scatter or peculiar velocity uncertainties may break the linearisation. For example, in Appendix D we show that an inflated intrinsic scatter of 0.15 mag would have produced a  $\sim 0.5\sigma$  bias in  $M_{H,1}^W$  for the combined sample. Desmond et al. (2025) lay out this interplay between selection and priors explicitly in a toy model for a distance-ladder inference of  $H_0$ , show-

ing that the cancellation between volume prior and selection holds exactly in the case of negligible redshift uncertainties and selection on redshift.

In this work we construct the first forward model of the MW Cepheid population that explicitly accounts for selection effects, models distance priors accurately, and infers the intrinsic population properties. The inferred period–luminosity relation parameters and *Gaia* parallax offset are consistent within  $1\sigma$  with, and of comparable precision to, both R21 and the baseline SH0ES result of R22. Our results highlight the importance of forward modelling and principled selection treatment, an approach set to become the standard for future distance-ladder (and other) analyses. Realising this programme requires well-defined observational campaigns with well-characterised selection functions, though the advent of simulation-based inference (SBI; Cranmer et al. 2020; Alsing et al. 2019) will in principle make even complex selection modelling tractable. In practice, SBI typically forward-simulates entire populations from population-level parameters, and the small sample sizes characteristic of the distance ladder make learning the likelihood surface from simulated catalogues challenging. A per-star forward model, as pursued here, remains the more natural approach for samples of this size.

The intrinsic scatter of the period–luminosity relation is another point of departure from R21, who adopt a fixed value of 0.06 mag motivated by the scatter of LMC Cepheids. We instead treat the scatter as a free parameter, inferring  $\sigma_{\text{int}}^{\text{C22}} = 0.071 \pm 0.022$  mag and  $\sigma_{\text{int}}^{\text{C27}} = 0.040 \pm 0.016$  mag in the fiducial model. The larger C22 value likely reflects residual extinction uncertainties along the sightlines to the more distant C22 Cepheids, though a period-dependent intrinsic scatter could also contribute given the longer periods of the C22 sample. As discussed in Section 4.1, allowing a free parallax uncertainty scaling  $f_{\varpi}$  yields  $f_{\varpi} = 1.23 \pm 0.16$  for the joint MW sample, consistent with the fixed factor of 1.1 adopted by R21, with negligible impact on the period–luminosity parameters.

The low scatter of the Cepheid period–luminosity relation and the high precision of the *HST* Wesenheit magnitudes provide a stringent test of the *Gaia* EDR3 parallaxes. Our tests of rescaling the parallax uncertainties yield  $f_{\varpi} = 1.24 \pm 0.18$  for C22 and  $f_{\varpi} = 0.71 \pm 0.33$  for C27, or  $f_{\varpi} = 1.23 \pm 0.16$  when modelling the two samples jointly (in which case the more distant C22 sample dominates the  $f_{\varpi}$  constraint), indicating that the *Gaia* uncertainties are reasonably estimated. This conclusion is consistent with that of R21, who found good agreement between model residuals and (10 per cent inflated) parallax errors, with a best  $\chi^2$  of 68 for 66 Cepheids. A similar result was reported by Ripepi et al. (2025), who found  $\chi_{\text{dof}}^2 \approx 1.04$  for this same *HST* sample. In contrast, Madore & Freedman (2026) report on noise in the *Gaia* EDR3 parallaxes of MW Cepheids based on photometry drawn from heterogeneous ground-based sources, stating “something subtle is amiss” regarding *Gaia* parallaxes. However, they do not quantify the significance of this statement or whether, or by how much, their residuals exceed the combined parallax and photometric uncertainties of the data, precluding a direct comparison with the results from *Gaia* presented here. We attempted to replicate their “qualine” colour analysis,  $Q = (V - I) - X(I - \text{NIR})$ , where NIR denotes a near-infrared photometric band and  $X$  is the

relevant reddening ratio. The measure of  $Q$  is noisy, as it combines the noise of four bands with a value of  $X > 1$  so that it is empirically equivalent to the noise of  $\sim 6$  bands added in quadrature. In contrast, the conventional Wesenheit of  $\text{NIR} - R(V - I)$ , where  $R \leq 0.4$ , has noise equivalent to  $\sim 1.5$  bands added in quadrature and thus is less demanding to measure. Specifically, we extended the period–luminosity model to include the qualine colour  $Q$  as an additional predictor, inferring its coefficient  $c_W$  jointly with all other parameters. For MW Cepheids and the LMC where  $Q$  can be reliably measured, we find  $c_W = -0.06 \pm 0.38$ , consistent with zero, with no evidence that residual colour information improves the calibration. At greater distances, the qualine colour becomes too noisy to measure usefully. The period–luminosity zero-point remains unchanged regardless of whether variations around the mean  $Q$  are included.

## 5.2 Comparison with Högäs & Mörtzell (2026)

HM26 claim that adopting physically motivated priors in the distance ladder reduces the Hubble tension from  $5\sigma$  to  $2\sigma$ . They extend the  $\chi^2$  model of R22 by treating MW Cepheids individually and sampling their distances as free parameters, rather than collapsing them into a single Gaussian constraint on the period–luminosity zero-point. Motivated by Desmond et al. (2025), they impose a uniform-in-volume distance prior,  $\pi(d) \propto d^2$ , on both the MW Cepheids and the nearby Cepheid host galaxies in the SH0ES sample. An equally fundamental point of Desmond et al. (2025), however, is that modelling selection is crucial: neglecting it biases the inference. HM26 entirely neglect this point, arguing that the MW Cepheid sample can be considered effectively complete because both *Gaia* and *HST* are capable of detecting Cepheids at much larger distances. This capability is beside the point. What matters is how the MW Cepheids in the SH0ES sample were actually selected: they are clearly confined to a limited distance range, and hence are not representative of the underlying population, which extends throughout the MW disk (and the Universe). The same argument applies to the nearby Cepheid host galaxies. Even if Type Ia supernovae are routinely detected at much larger distances, the question is why these particular nearby galaxies were selected for Cepheid observations—a selection effect that must be modelled, as done by Stiskalek et al. (2026). Indeed, Desmond et al. (2025) showed that even for a volume-limited sample—one that is complete out to a fixed true distance (rather than observed quantities like redshift or magnitude)—the selection must be accounted for by restricting the distance prior to the same range. An improper  $d^2$  prior that extends beyond the sample boundary biases the inference even in that case. The mechanism is straightforward: a uniform-in-volume prior assigns increasing weight to large distances through the  $d^2$  volume factor, but the selection excludes stars beyond a certain range. Without modelling the selection, the inference overweights distant Cepheids, shifting the period–luminosity zero-point to brighter values and  $\delta_{\varpi}$  to more negative values.

HM26 report a marginalised posterior of  $M_{H,1}^W = -5.959 \pm 0.018$  mag and  $\delta_{\varpi} = -26.2 \pm 5.0 \mu\text{s}$  (their figure 2). This brighter zero-point relative to the baseline SH0ES value of  $-5.894$  mag implies a larger distance scale, yielding  $H_0 = 70.6 \pm 1.0 \text{ km s}^{-1} \text{ Mpc}^{-1}$ . This result is driven

by their neglect of selection effects. Of our analysis variants, the one most closely resembling their approach—a uniform-in-volume prior with no selection modelling and a wide prior on  $\delta_\varpi$ , using MW, LMC, and N4258 Cepheids—yields  $M_{H,1}^W = -5.982 \pm 0.023$  mag and  $\delta_\varpi = -36.3 \pm 6.1$   $\mu\text{as}$ , in reasonable agreement with them. The residual difference is likely attributable to two factors: we model the Cepheid population hyperprior, and their global fit includes the remainder of the distance ladder, which, while lacking a geometric distance calibration, may still mildly pull the period–luminosity parameters and  $\delta_\varpi$ . Modelling selection, as we do in this work, shifts the Cepheid zero-point back toward the baseline SH0ES value and consequently pushes  $H_0$  back up (Section 5.3).

In Fig. 6 we present PPCs for our fiducial model. When selection is included, the predicted distributions of  $m_H^W$ ,  $\varpi_{\text{obs}}$ , and  $\log P_{\text{obs}}$  closely match the observed data. Without selection modelling, the predicted distributions of both  $m_H^W$  and  $\varpi_{\text{obs}}$  are incompatible with the observations. The degree of this incompatibility depends on the range of the distance prior: we adopt  $d_{\text{min}} = 0.1$  kpc for both samples and  $d_{\text{max}} = 8.5$  kpc and  $d_{\text{max}} = 2.0$  kpc for the C22 and C27 samples, respectively, somewhat larger than the most distant Cepheid in each. Extending  $d_{\text{max}}$  further would worsen the disagreement, as the model would predict Cepheids at distances where none are observed. This connects directly to the selection argument above. Even for the C27 sample, where the dominant selection is in parallax and therefore approximately in distance, completeness up to some maximum distance does not obviate the need for selection modelling. That maximum distance must be explicitly encoded, e.g., in the prior; otherwise the inference assigns non-negligible probability to distances beyond the threshold, allowed by the likelihood but completely excluded by the selection.

The close agreement between our Bayesian forward model and the SH0ES parallax-space  $\chi^2$  analysis is interesting. The two approaches differ fundamentally: SH0ES calibrates directly in parallax space without sampling distances, imposing a spatial prior, or explicitly modelling selection. In Appendix D we show analytically that the per-star likelihood of the forward model, after marginalising over the latent distance under a power-law prior and locally linearising the distance modulus, reduces to a Gaussian in parallax space whose exponent matches the  $\chi^2$ . Depending on whether the selection acts in parallax or in magnitude, different prefactors multiply the exponential, but these are effectively constant or negligible when the intrinsic scatter of the period–luminosity relation is small, i.e. when the parallax measurement uncertainty dominates the error budget, as is the case for MW Cepheids. In this regime, the Bayesian forward model reduces effectively to a weighted regression in parallax space conditional on the observed sample. Mock bias tests (Appendix E) confirm that, at the fiducial scatter of  $\sigma_{\text{int}} \approx 0.06$  mag, consistent with the value inferred from the data, the linearised Gaussian and  $\chi^2$  methods are only mildly biased; only where the scatter  $\gtrsim 0.15$  mag would the  $\chi^2$  method be significantly biased (the Bayesian forward model is unbiased in all cases).

The consistency of the inferred period–luminosity parameters across methods therefore follows from the small intrinsic scatter of MW Cepheids, and demonstrates that the larger shift introduced by a uniform-in-volume prior without

selection modelling, as adopted by HM26, is a consequence of a poor generative model of the data. Because the intrinsic scatter is small, the per-star likelihood sharply constrains the distance, rendering the prior approximately constant over the relevant interval; its effective value is set by the peak location, which depends on the model parameters. When the selection function is included in the posterior, these per-star prior factors approximately cancel against the selection normalisation, as shown in Appendix D under the linearisation of the distance modulus, and the functional form of the prior has negligible impact on the inferred parameters. Without selection modelling, however, the prior factors evaluated at different parameter-dependent distances for different stars no longer cancel, and the inference becomes biased. This is shown by the adoption of a uniform-in-volume prior without modelling of the selection function producing posterior predictive distributions of observables clearly discrepant with the data (Fig. 6).

While not important for our main argument, we also note a spurious asymmetry in HM26’s treatment of the second and third rungs of the distance ladder. They impose a uniform-in-volume prior on MW Cepheids and nearby Cepheid host galaxies, yet for the Hubble flow supernovae they retain the  $\chi^2$  treatment of R22. They argue that the BEAMS with Bias Corrections method (BBC; Popovic et al. 2021), while correcting SN Ia distance moduli for observational selection effects and standardisation biases, operates at the level of SN Ia standardisation and is not designed to compensate for assumptions about distance priors in the calibration of the local distance ladder. On this basis they dismiss the suggestion of Desmond et al. (2025) that BBC may already compensate for the use of a flat prior on distance modulus. If this is the case, and BBC does not effectively account for the distance prior, then a uniform-in-volume prior should have been applied to the Hubble-flow hosts as well, yet HM26 do not do so. They motivate this by noting that Hubble-flow distances can be viewed as derived quantities ( $d = cz/H_0$ ) rather than free parameters, so that a uniform-in-volume prior on them would translate into a prior on  $H_0$  itself. This is unconvincing: by the same reasoning, any distance in the ladder could be recast as a derived quantity, and no distance prior would ever be required. There is no reason why a prior on distances should not translate to an effective prior on  $H_0$ , which is precisely what happens in the rest of the model anyway when marginalising over the latent distances.

### 5.3 Implications for the Hubble constant

Our full Bayesian forward model is restricted to the calibration of the first rung of the distance ladder (Cepheids), although the consequences for the full distance ladder inference of  $H_0$  are clear. Given that the Cepheid period–luminosity relation parameters we infer are consistent with the baseline SH0ES values, we expect modifications to the SH0ES  $H_0$  value to be marginal and the Hubble tension to remain at  $\sim 5\sigma$ . To verify this, we replicate the  $\chi^2$  analysis of the full distance ladder of R22, recovering  $H_0 = 73.04 \pm 1.01$  km s $^{-1}$  Mpc $^{-1}$ , matching their reported value. R22 constrain the period–luminosity zero-point using both *HST* and *Gaia* parallaxes, obtaining  $M_{H,1}^W = -5.804 \pm 0.082$  mag and  $M_{H,1}^W = -5.903 \pm 0.025$  mag, respectively. These con-

straints are derived from partially overlapping sets of MW Cepheids observed with two independent astrometric instruments; the per-star error budget is dominated by the parallax uncertainties ( $\sim 0.14$  mag for *Gaia*,  $\sim 0.35$  mag for *HST*), which are independent, minimising the correlation between the two constraints. We consider dropping the *HST* constraint and retaining only the *Gaia* one, which yields  $H_0 = 72.91 \pm 1.01 \text{ km s}^{-1} \text{ Mpc}^{-1}$ , a negligible shift. Replacing the *Gaia* constraint with the zero-point inferred in this work yields  $H_0 = 73.12 \pm 1.08 \text{ km s}^{-1} \text{ Mpc}^{-1}$ . These shifts are at most  $\sim 0.1\sigma$ , confirming that our inferred Cepheid zero-point leaves the Hubble tension intact. This  $\chi^2$ -based estimate is only illustrative, as it grafts our Bayesian zero-point onto the frequentist framework of R22; we leave a fully consistent Bayesian reanalysis of the complete distance ladder to future work. We similarly expect a negligible impact on the two-rung Bayesian distance ladder of Stiskalek et al. (2026), who used the same MW constraints as R22.

#### 5.4 Limitations of this work

For the C27 sample, the reported selection cuts alone suffice to reproduce the observed distributions in a PPC (Fig. 6). We additionally introduce a mild selection term on the Wesenheit magnitude, in place of a *V*-band cut to avoid *HST* saturation, to remove the brightest Cepheids, though this has a negligible effect on the inferred parameters.

The C22 sample presents greater challenges. It was drawn from a parent catalogue of MW Cepheids with an implicit completeness limit  $V \lesssim 15$  mag, to which three explicit cuts were applied: a period cut  $P > 8$  days, an extinction cut  $A_H < 0.4$  mag, and a saturation cut  $V > 6$  mag. We implement the period and extinction cuts, but these alone do not reproduce the observed distributions of magnitude and parallax. We therefore introduce additional smooth selection terms on the Wesenheit magnitude and observed parallax. The parallax selection dominates; results would be near-indistinguishable had we neglected the Wesenheit magnitude term. This therefore constitutes an effective selection function, not identical to the reported cuts, and can potentially be understood as partially modelling the selection of the parent sample population itself. The inferred thresholds yield a PPC that closely reproduces the observed distributions (Fig. 6).

The parent sample selection is complicated by the fact that it operates on the *V*-band magnitude, whereas our forward model predicts the Wesenheit magnitude. Modelling the *V*-band selection self-consistently would require predicting *V*-band magnitudes and hence modelling the period–luminosity relation in that band, with its own intrinsic scatter correlated with the Wesenheit scatter (see Yasin et al. 2026 for such a treatment of correlated scatter in galaxy cluster scaling relations). While in principle straightforward, this would require extending the framework to multiple bands simultaneously. We instead adopt the simpler approach of modelling an effective selection in Wesenheit magnitude with a smooth cut, even though the data were never selected on this quantity. Since the *V*-band and Wesenheit magnitudes are strongly correlated, a smooth cut in the latter can effectively mimic a cut in the former.

A further limitation concerns the modelling of selection associated with extinction. The C22 sample was subject to

an explicit cut  $A_H < 0.4$  mag, but modelling this selection requires knowing the extinction not only along the observed sightlines but in principle at all positions in the Galaxy. We use the **Bayestar19** three-dimensional dust map (Green et al. 2019), supplemented by the Marshall et al. (2006) map for sightlines where **Bayestar19** lacks coverage; however, the standard deviation of the inter-map differences for the C22 Cepheids is 0.08 mag, and no existing map provides reliable extinctions throughout the Galactic plane. Moreover, the definition of the Wesenheit magnitude assumes a fixed extinction law; Skowron et al. (2026) show that spatial  $R_V$  variations across the MW disk can shift the *Gaia*-based Wesenheit index  $W_G$  by up to  $\sim 0.7$  mag, though the near-infrared  $m_H^W$  used here is far less sensitive. Given these systematic uncertainties, the fiducial C22 selection does not include the extinction cut. When the LMC and N4258 are included, enabling the extinction selection has a negligible effect on the period–luminosity parameters ( $\Delta M_{H,1}^W = 0.008$  mag); without anchors, the effect is larger, but the inference is in any case poorly constrained (Appendix B). The C27 Cepheids are too nearby for extinction selection to matter. The C22 campaign analysed alone prefers a mildly positive parallax offset ( $\delta_\varpi = +1 \pm 7 \mu\text{as}$ ), in tension with the negative values favoured by our fiducial analysis; this drives the zero-point faintward. Including the LMC and N4258 resolves this tension by effectively anchoring the period–luminosity relation independently of the MW parallaxes.

## 6 CONCLUSION

We have presented a Bayesian forward model of the MW Cepheid population that jointly infers the period–luminosity relation parameters, the *Gaia* parallax zero-point offset, and the intrinsic population distributions, while marginalising over the distances and latent true periods and metallicities of individual Cepheids and explicitly accounting for the sample selection function and the disk geometry of the MW. Combined with geometric calibration of the LMC and N4258, our fiducial model yields a period–luminosity zero-point of  $M_{H,1}^W = -5.909 \pm 0.022$  mag and a *Gaia* parallax offset of  $\delta_\varpi = -12.4 \pm 5.3 \mu\text{as}$ ; the zero-point is consistent within  $0.7\sigma$  with the baseline SH0ES value. Neglecting the selection function and adopting a uniform-in-volume prior shifts  $M_{H,1}^W$  brighter by  $\sim 0.05$  mag and  $\delta_\varpi$  more negative by  $\sim 14 \mu\text{as}$ , demonstrating that principled selection modelling is essential for unbiased inference. The reduced Hubble tension reported by HM26 is an artefact of this neglect: applying a uniform-in-volume prior without accounting for the selection that defines the sample biases the zero-point bright and  $H_0$  low (see also Desmond et al. 2025). The apparent mitigation of the Hubble tension in HM26 therefore arises from modelling assumptions that fail to match the generating process of the data, not from new information.

This work is part of a larger programme to forward-model the full distance ladder in a statistically rigorous way. Stiskalek et al. (2026) developed the framework for the second rung—the Cepheid host galaxies—and showed that, when coupled with the **Manticore-Local** model of the local Universe (McAlpine et al. 2025), which accounts for galaxy bias and peculiar velocities,  $H_0$  can be inferred with-

out supernovae at  $\sim 1.8\%$  precision from as few as 35 host galaxies. The present work extends the programme to the first rung, treating the MW calibration self-consistently. The remaining piece is the third rung: applying a similar approach to the Type Ia supernovae and performing end-to-end Bayesian inference from geometric anchors to the Hubble flow. Feeney et al. (2018) pursued this goal but adopted a uniform-in-distance-modulus prior and neglected the selection function. Modelling Type Ia supernova selection is particularly challenging, as it depends on discovery magnitude, light-curve colour and stretch, host-galaxy properties, and survey-specific targeting strategies, among others (Kessler & Scolnic 2017; Popovic et al. 2021; Boyd et al. 2024).

More broadly, the framework we develop extends beyond the Cepheid–supernova ladder. Alternative distance indicators such as the tip of the red giant branch, surface brightness fluctuations, and masers can be treated analogously, provided their selection is well understood, and can independently challenge or corroborate the Hubble tension. Looking beyond current data, such forward modelling will be particularly compelling when applied to dedicated observational campaigns collecting samples with well-defined selection criteria that can be modelled cleanly—rather than to archival data with heterogeneous selection criteria, as is currently the case.

## 7 DATA AVAILABILITY

The C22 and C27 data used in this work were extracted from table 1 of R22. The SH0ES data are available at [github.com/PantheonPlusSH0ES/DataRelease](https://github.com/PantheonPlusSH0ES/DataRelease). The code and all other data will be made available on reasonable request to the authors.

## ACKNOWLEDGEMENTS

We thank Pedro G. Ferreira for useful inputs and discussions. RS acknowledges financial support from STFC Grant No. ST/X508664/1, and the Snell Exhibition of Balliol College, Oxford. HD is supported by a Royal Society University Research Fellowship (grant no. 211046).

The authors would like to acknowledge the use of the University of Oxford Advanced Research Computing (ARC) facility in carrying out this work<sup>4</sup>.

## REFERENCES

- Alsing J., Charnock T., Feeney S., Wandelt B., 2019, *MNRAS*, **488**, 4440
- Bartlett D. J., Desmond H., 2023, *The Open Journal of Astrophysics*, **6**, 42
- Bhardwaj A., et al., 2021, *ApJ*, **909**, 200
- Bhardwaj A., et al., 2023, *ApJ*, **955**, L13
- Bidenko B., Koopmans L. V. E., Meerburg P. D., 2023, *arXiv e-prints*, p. [arXiv:2308.05157](https://arxiv.org/abs/2308.05157)
- Bobylev V. V., Bajkova A. T., 2021, *Astronomy Letters*, **47**, 534
- Boyd B. M., Grayling M., Thorp S., Mandel K. S., 2024, *arXiv e-prints*, p. [arXiv:2407.15923](https://arxiv.org/abs/2407.15923)
- Breival L., Riess A. G., Kervella P., Anderson R. I., Romaniello M., 2022, *ApJ*, **939**, 89
- Breival L., et al., 2025, *ApJ*, **994**, 111
- Camphuis E., et al., 2025, *arXiv e-prints*, p. [arXiv:2506.20707](https://arxiv.org/abs/2506.20707)
- Cardona W., Kunz M., Pettorino V., 2017, *J. Cosmology Astropart. Phys.*, **2017**, 056
- Cranmer K., Brehmer J., Louppe G., 2020, *Proceedings of the National Academy of Science*, **117**, 30055
- Cruz Reyes M., Anderson R. I., 2023, *A&A*, **672**, A85
- Delgado H. E., Sarro L. M., Clementini G., Muraveva T., Garofalo A., 2019, *A&A*, **623**, A156
- Desmond H., Stiskalek R., Najera J. A., Banik I., 2025, *arXiv e-prints*, p. [arXiv:2511.03394](https://arxiv.org/abs/2511.03394)
- Di Valentino E., et al., 2025, *Physics of the Dark Universe*, **49**, 101965
- Ding Y., Liao S., Wen S., Qi Z., 2025, *AJ*, **169**, 211
- Drimmel R., Khanna S., Poggio E., Skowron D. M., 2025, *A&A*, **698**, A230
- Efstathiou G., 2021, *MNRAS*, **505**, 3866
- Fabrizius C., et al., 2021, *A&A*, **649**, A5
- Feeney S. M., Mortlock D. J., Dalmaso N., 2018, *MNRAS*, **476**, 3861
- Freedman W. L., Madore B. F., Hoyt T. J., Jang I. S., Lee A. J., Owens K. A., 2025, *ApJ*, **985**, 203
- GRAVITY Collaboration 2019, *Astronomy & Astrophysics*, **625**, L10
- Gaia Collaboration Brown A. G. A., Vallenari A., Prusti T., de Bruijne J. H. J., Babusiaux C., Biermann M., 2021, *Astronomy & Astrophysics*, **649**, A1
- Gieren W., et al., 2018, *A&A*, **620**, A99
- Green G. M., 2018, *The Journal of Open Source Software*, **3**, 695
- Green G. M., Schlafly E., Zucker C., Speagle J. S., Finkbeiner D., 2019, *ApJ*, **887**, 93
- Groenewegen M. A. T., 2021, *A&A*, **654**, A20
- Groenewegen M. A. T., 2023, *A&A*, **669**, A4
- H0DN Collaboration et al., 2025, *arXiv e-prints*, p. [arXiv:2510.23823](https://arxiv.org/abs/2510.23823)
- Hoffman M. D., Gelman A., 2011, *arXiv e-prints*, p. [arXiv:1111.4246](https://arxiv.org/abs/1111.4246)
- Högas M., Mörtzell E., 2026, *arXiv e-prints*, p. [arXiv:2601.22215](https://arxiv.org/abs/2601.22215)
- Huang Y., Yuan H., Beers T. C., Zhang H., 2021, *ApJ*, **910**, L5
- Kelly B. C., 2007, *The Astrophysical Journal*, **665**, 1489
- Kessler R., Scolnic D., 2017, *ApJ*, **836**, 56
- Kushnir D., Sharon A., 2025, *MNRAS*, **538**, 2838
- Lindgren L., et al., 2021, *A&A*, **649**, A4
- Louis T., La Posta A., Atkins Z., Jense H. T., Abril-Cabezas I., Addison G. E., Ade P. A. R., et al., 2025, *J. Cosmology Astropart. Phys.*, **2025**, 062
- Madore B. F., 1982, *ApJ*, **253**, 575
- Madore B. F., Freedman W. L., 2026, *arXiv e-prints*, p. [arXiv:2602.13397](https://arxiv.org/abs/2602.13397)
- Madore B. F., Freedman W. L., Owens K., 2025, *ApJ*, **981**, 32
- Marshall D. J., Robin A. C., Reylé C., Schultheis M., Picaud S., 2006, *A&A*, **453**, 635
- McAlpine S., Jasche J., Ata M., Lavaux G., Stiskalek R., Frenk C. S., Jenkins A., 2025, *MNRAS*, **540**, 716
- Molinaro R., et al., 2023, *MNRAS*, **520**, 4154
- Mörtzell E., Goobar A., Johansson J., Dhawan S., 2022, *ApJ*, **933**, 212
- Nunnari A., et al., 2025, *arXiv e-prints*, p. [arXiv:2511.22491](https://arxiv.org/abs/2511.22491)
- Phan D., Pradhan N., Jankowiak M., 2019, *arXiv e-prints*, p. [arXiv:1912.11554](https://arxiv.org/abs/1912.11554)
- Pietrzyński G., et al., 2019, *Nature*, **567**, 200
- Planck Collaboration et al., 2020, *A&A*, **641**, A6
- Popovic B., Brout D., Kessler R., Scolnic D., Lu L., 2021, *ApJ*, **913**, 49
- Reid M. J., Pesce D. W., Riess A. G., 2019, *The Astrophysical Journal Letters*, **886**, L27

<sup>4</sup> [doi.org/10.5281/zenodo.22558](https://doi.org/10.5281/zenodo.22558)

- Riess A. G., et al., 2016, *The Astrophysical Journal*, 826, 56
- Riess A. G., Casertano S., Yuan W., Bowers J. B., Macri L., Zinn J. C., Scolnic D., 2021, *The Astrophysical Journal Letters*, 908, L6
- Riess A. G., et al., 2022a, *The Astrophysical Journal Letters*, 934, L7
- Riess A. G., et al., 2022b, *ApJ*, 938, 36
- Riess A. G., et al., 2024, *ApJ*, 962, L17
- Riess A. G., et al., 2025, *ApJ*, 992, L34
- Ripepi V., et al., 2025, *arXiv e-prints*, p. arXiv:2508.17447
- Romaniello M., et al., 2022, *Astronomy & Astrophysics*, 658, A29
- Samus' N. N., Kazarovets E. V., Durlevich O. V., Kireeva N. N., Pastukhova E. N., 2017, *Astronomy Reports*, 61, 80
- Skowron D. M., Drimmel R., Khanna S., Spagna A., Poggio E., Ramos P., 2025, *ApJS*, 278, 57
- Skowron D. M., Fouesneau M., Drimmel R., Khanna S., 2026, *ApJ*, 998, L9
- Stassun K. G., Torres G., 2021, *ApJ*, 907, L33
- Stiskalek R., Desmond H., Tsaprazi E., Heavens A., Lavaux G., McAlpine S., Jasche J., 2026, *MNRAS*, 546, staf2260
- Tammann G. A., Sandage A., Reindl B., 2003, *A&A*, 404, 423
- Tully R. B., et al., 2023, *ApJ*, 944, 94
- Udalski A., Szymanski M., Kaluzny J., Kubiak M., Mateo M., 1992, *Acta Astronomica*, 42, 253
- Verde L., Schöneberg N., Gil-Marín H., 2024, *ARA&A*, 62, 287
- Yasin T., Stiskalek R., Desmond H., von Hausegger S., Ferreira P. G., 2026, *arXiv e-prints*, p. arXiv:2602.06007
- Zinn J. C., 2021, *AJ*, 161, 214
- da Silva R., et al., 2022, *A&A*, 661, A104

## APPENDIX A: SPIRAL ARM MODULATION OF THE DISTANCE PRIOR

MW Cepheids are young stars that trace the Galactic spiral structure. The axisymmetric disk prior of Eq. (2) does not capture this azimuthal dependence and may therefore assign non-negligible probability to inter-arm regions where few Cepheids reside. We optionally modulate the disk prior with a spiral arm density profile to test whether accounting for this structure affects the inferred parameters.

We adopt the four-arm log-periodic spiral model of Drimmel et al. (2025), derived from 2857 classical Cepheids with WISE mid-infrared distances (Skowron et al. 2025). The four arms—Scutum, Sagittarius–Carina, Local (Orion), and Perseus—are each described by a trace in the Galactic plane, parametrised as

$$\ln R = \ln R_{0,k} - \tan \psi_k \phi, \quad (\text{A1})$$

where  $R$  is the Galactocentric radius,  $\phi$  the azimuthal angle,  $R_{0,k}$  the reference radius, and  $\psi_k$  the pitch angle of the  $k^{\text{th}}$  arm.

The spiral-modulated prior is the joint position density of Eq. (2) scaled by a factor that enhances the density near the arm traces:

$$\pi(d_i, \ell_i, b_i) \propto \pi_{\text{disk}}(d_i, \ell_i, b_i) \mathcal{S}_{\text{arm}}(d_i, \ell_i, b_i), \quad (\text{A2})$$

where the spiral modulation factor is

$$\mathcal{S}_{\text{arm}} = (1 - f_{\text{arm}}) + f_{\text{arm}} \sum_{k=1}^4 \exp\left(-\frac{\Delta_k^2}{2\sigma_{\text{arm}}^2}\right), \quad (\text{A3})$$

$\pi_{\text{disk}}$  is the joint position density of Eq. (2),  $\Delta_k(d_i, \ell_i, b_i)$  is the projected distance in the Galactic plane from the Cepheid to the nearest point on the  $k^{\text{th}}$  arm trace,  $f_{\text{arm}} \in$

$[0, 1]$  is the fraction of the Cepheid surface density attributed to spiral arms, and  $\sigma_{\text{arm}}$  is the Gaussian arm width. When  $f_{\text{arm}} = 0$ , the spiral factor reduces to unity and the axisymmetric disk prior is recovered. At the opposite limit  $f_{\text{arm}} = 1$ , the prior is concentrated entirely on the arm traces. Both  $f_{\text{arm}}$  and  $\sigma_{\text{arm}}$  are sampled as free parameters:  $f_{\text{arm}}$  with a uniform prior on  $[0, 1]$  and  $\sigma_{\text{arm}}$  with a half-normal prior  $\mathcal{N}^+(0.3, 0.2^2)$  kpc, truncated at zero.

The nearest-point distances  $\Delta_k$  are computed by converting the heliocentric coordinates  $(d_i, \ell_i, b_i)$  to Galactocentric Cartesian coordinates  $(x_{\text{GC}}, y_{\text{GC}})$  in the midplane and querying a KD-tree built from the densified arm traces and querying the squared distances  $\Delta_k^2$  for each sightline on a fine distance grid are precomputed and cached; at inference time, the spiral factor is evaluated by interpolating  $\Delta_k^2$  to the sampled distance  $d_i$ . The prior of Eq. (A2) is normalised numerically per sightline via Simpson's rule on the same grid. An analogous precomputation is performed for the Monte Carlo sightlines entering the detection probability of Eq. (39), ensuring that the spiral modulation propagates consistently into both the per-star prior and the selection modelling. As reported in Table 4, the spiral-arm-modulated prior leaves the posteriors virtually unchanged relative to the axisymmetric disk prior.

## APPENDIX B: INDIVIDUAL CAMPAIGN RESULTS

Table B1 reports posteriors for the C22 and C27 campaigns analysed separately, each combined with the LMC and N4258; Fig. B1 shows the corresponding corner plots. The LMC and N4258 are required to break the  $M_{H,1}^W - \delta_{\varpi}$  degeneracy inherent in parallax-only data, so we include them throughout.

With the LMC and N4258—which dominate the constraint on  $M_{H,1}^W$ —the two campaigns yield consistent zero-points:  $M_{H,1}^W = -5.865 \pm 0.026$  mag (C22) and  $-5.916 \pm 0.024$  mag (C27), differing by  $1.4\sigma$ . The slopes and metallicity coefficients, likewise dominated by the LMC and N4258 data, agree to within  $0.5\sigma$ . Both individual-campaign zero-points are consistent with the joint C22 + C27 result of  $M_{H,1}^W = -5.909 \pm 0.022$  mag (Table 4), confirming that the two campaigns carry no internal tension. Selection modelling has a larger effect on C22 than on C27: disabling the selection function shifts  $M_{H,1}^W$  by 0.040 mag and  $\delta_{\varpi}$  by 11  $\mu\text{as}$  for C22, compared with 0.008 mag and 6  $\mu\text{as}$  for C27. This is expected, as the more distant C22 sample is more strongly affected by magnitude truncation. Similarly, the nearby C27 Cepheids ( $d \lesssim 1.25$  kpc,  $\varpi \gtrsim 800$   $\mu\text{as}$ ) are largely insensitive to the parallax offset: for  $\delta_{\varpi} = -10$   $\mu\text{as}$ , the induced distance modulus shift is only  $\sim 0.02$  mag, compared with  $\sim 0.07$  mag for the typical C22 parallax of  $\sim 300$   $\mu\text{as}$ . The constraint on  $\delta_{\varpi}$  is therefore driven by the more distant C22 sample.

The fiducial C22 selection does not include the extinction cut  $A_H < 0.4$  mag, owing to the systematic uncertainties in three-dimensional dust maps discussed in Section 5.4. With the LMC and N4258 included, enabling the extinction selection has a negligible effect on the period–luminosity parameters ( $\Delta M_{H,1}^W = 0.008$  mag), but the inferred scatter in-

creases, consistent with residual extinction along the more distant C22 sightlines. The R21  $\chi^2$  rows apply the frequentist  $\chi^2$  method with intrinsic scatter fixed at 0.06 mag.

### APPENDIX C: PER-STAR DISTANCE COMPARISON

The forward model samples a distance  $d_i$  for each MW Cepheid. Converting these to distance moduli  $\mu_{\text{forward},i} = 5 \log(d_i/\text{kpc}) + 10$  provides a direct comparison with the photometric distance moduli  $\mu_{\text{SH0ES}}$  predicted from the baseline SH0ES period–luminosity parameters ( $M_{H,1}^W = -5.894$  mag,  $b_W = -3.299$ ,  $Z_W = -0.217$ ). Figure C1 shows the per-star residuals  $\langle \mu_{\text{forward}} \rangle - \mu_{\text{SH0ES}}$  for both the MW-only and fiducial models. The residuals scatter about zero with only a minor systematic offset. Including the LMC and N4258 tightens the period–luminosity relation but does not shift the per-star distance posteriors.

Figure C2 shows the distribution of the posterior-mean residuals from the fiducial C22 + C27 + LMC + N4258 inference, split by campaign. The C22 residuals have a mean offset of +0.004 mag with a standard deviation of 0.042 mag, while the C27 residuals have a mean of +0.025 mag and a standard deviation of 0.030 mag. The positive C27 offset is expected: the reference  $\mu_{\text{SH0ES}}$  is computed from the baseline SH0ES zero-point ( $M_{H,1}^W = -5.894$  mag), which is 0.015 mag fainter than our fiducial value ( $M_{H,1}^W = -5.909$  mag), predicting systematically shorter SH0ES distances and hence positive residuals.

### APPENDIX D: SIMILARITY OF THE FORWARD MODEL AND THE $\chi^2$ METHOD

Here we derive the relation between the forward model of Section 3 and the  $\chi^2$  treatment of R21. For simplicity, we treat the period and metallicity as known quantities with no population prior or selection, so that neither requires marginalisation; since they enter the Gaussian likelihood linearly, they could be marginalised analytically under a Gaussian population prior as in the main text. The per-star likelihood for a single MW Cepheid at distance  $d$  then reduces to

$$\mathcal{L}(m_{H,\text{obs}}^W, \varpi_{\text{obs}} | d, \boldsymbol{\theta}) = \mathcal{N}(m_{H,\text{obs}}^W | M + \mu(d), \sigma_1^2) \times \mathcal{N}(\varpi_{\text{obs}} | 1/d - \delta_\varpi, \sigma_\varpi^2), \quad (\text{D1})$$

where  $M \equiv M_{H,1}^W + b_W(\log P - 1) + Z_W [\text{O}/\text{H}]$  is the predicted absolute magnitude,  $\sigma_1^2 = \sigma_m^2 + \sigma_{\text{int}}^2$  is the total magnitude variance, and  $\mu(d) = 5 \log(d/10 \text{ pc})$  is the distance modulus. Adopting a uniform-in-volume distance prior,  $\pi(d) \propto d^2$ , the marginal likelihood is

$$\mathcal{L}^{\text{marg}}(m_{H,\text{obs}}^W, \varpi_{\text{obs}} | \boldsymbol{\theta}) \propto \int dd d^2 \times \mathcal{N}(m_{H,\text{obs}}^W | M + \mu(d), \sigma_1^2) \mathcal{N}(\varpi_{\text{obs}} | 1/d - \delta_\varpi, \sigma_\varpi^2). \quad (\text{D2})$$

Changing variables to  $\varpi = 1/d - \delta_\varpi$ , so that  $d = 1/(\varpi + \delta_\varpi)$  and  $|dd| = d\varpi/(\varpi + \delta_\varpi)^2$ , the parallax likelihood simplifies

and the integral becomes

$$\mathcal{L}^{\text{marg}} \propto \int d\varpi (\varpi + \delta_\varpi)^{-4} \mathcal{N}(m_{H,\text{obs}}^W | M + \mu(\varpi), \sigma_1^2) \times \mathcal{N}(\varpi_{\text{obs}} | \varpi, \sigma_\varpi^2), \quad (\text{D3})$$

where  $\mu(\varpi) = -5 \log(\varpi + \delta_\varpi) + 10$ . Following the main text, we define the photometric parallax as the geometric parallax corresponding to the photometric distance,

$$\varpi_{\text{phot}} = 10^{-0.2(m_{H,\text{obs}}^W - M - 10)}. \quad (\text{D4})$$

In the  $\varpi$  coordinate, the magnitude likelihood peaks at  $\varpi = \varpi_{\text{phot}} - \delta_\varpi$ , since  $\mu(\varpi) = m_{H,\text{obs}}^W - M$  when  $\varpi + \delta_\varpi = \varpi_{\text{phot}}$ .

To marginalise Eq. (D3) analytically, we linearise  $\mu(\varpi)$  around  $\varpi_{\text{phot}} - \delta_\varpi$ . Since

$$\frac{d\mu}{d\varpi} = -\frac{5}{\ln 10 (\varpi + \delta_\varpi)}, \quad (\text{D5})$$

a first-order Taylor expansion gives

$$\mu(\varpi) \approx \mu(\varpi_{\text{phot}} - \delta_\varpi) - \frac{5}{\ln 10} \frac{\varpi - \varpi_{\text{phot}} + \delta_\varpi}{\varpi_{\text{phot}}}. \quad (\text{D6})$$

Substituting into the magnitude likelihood and using  $m_{H,\text{obs}}^W = M + \mu(\varpi_{\text{phot}} - \delta_\varpi)$ , the residual is

$$m_{H,\text{obs}}^W - M - \mu(\varpi) \approx \frac{5}{\ln 10} \frac{\varpi - \varpi_{\text{phot}} + \delta_\varpi}{\varpi_{\text{phot}}}. \quad (\text{D7})$$

The magnitude Gaussian becomes

$$\mathcal{N}(m_{H,\text{obs}}^W | M + \mu(\varpi), \sigma_1^2) \approx \frac{\sigma_{\varpi,m}}{\sigma_1} \mathcal{N}(\varpi | \varpi_{\text{phot}} - \delta_\varpi, \sigma_{\varpi,m}^2), \quad (\text{D8})$$

where the uncertainty in ‘‘parallax space’’ after the linearisation is

$$\sigma_{\varpi,m} = \frac{\ln 10}{5} \varpi_{\text{phot}} \sigma_1. \quad (\text{D9})$$

Expanding the volume-prior factor around  $\varpi_{\text{phot}} - \delta_\varpi$ ,

$$(\varpi + \delta_\varpi)^{-4} \approx \varpi_{\text{phot}}^{-4} \left[ 1 - \frac{4(\varpi - \varpi_{\text{phot}} + \delta_\varpi)}{\varpi_{\text{phot}}} \right]. \quad (\text{D10})$$

The first-order correction is suppressed by the Gaussian likelihood centred on  $\varpi_{\text{phot}} - \delta_\varpi$  and we drop it. With this, the marginal likelihood reduces to a product of two Gaussians in  $\varpi$ ,

$$\mathcal{L}^{\text{marg}} \propto \varpi_{\text{phot}}^{-3} \times \int d\varpi \mathcal{N}(\varpi_{\text{obs}} | \varpi, \sigma_\varpi^2) \mathcal{N}(\varpi | \varpi_{\text{phot}} - \delta_\varpi, \sigma_{\varpi,m}^2), \quad (\text{D11})$$

which evaluates to

$$\mathcal{L}^{\text{marg}} \propto \varpi_{\text{phot}}^{-3} \mathcal{N}(\varpi_{\text{obs}} | \varpi_{\text{phot}} - \delta_\varpi, \tilde{\sigma}_\varpi^2), \quad (\text{D12})$$

with

$$\tilde{\sigma}_\varpi^2 \equiv \left( \frac{\ln 10}{5} \right)^2 \varpi_{\text{phot}}^2 \sigma_1^2 + \sigma_\varpi^2. \quad (\text{D13})$$

The Gaussian exponent  $(\varpi_{\text{obs}} - \varpi_{\text{phot}} + \delta_\varpi)^2 / \tilde{\sigma}_\varpi^2$  recovers the R21  $\chi^2$  of Eq. (49), and  $\tilde{\sigma}_\varpi$  matches Eq. (50) upon identifying  $\sigma_\varpi$  with  $\alpha \sigma_{\varpi,\text{EDR3}}$  and  $\sigma_1$  with  $\sigma_{m,\text{tot}}$ . We now consider the selection function term.

Model	$M_{H,1}^W$	$b_W$	$Z_W$	$\delta_\varpi$ [ $\mu\text{as}$ ]
<b>C22 + LMC + N4258</b>				
Disk prior, selection modelling	$-5.865 \pm 0.026$	$-3.309 \pm 0.032$	$-0.08 \pm 0.11$	$-6 \pm 6$
Disk prior, no selection	$-5.905 \pm 0.027$	$-3.320 \pm 0.032$	$-0.19 \pm 0.12$	$-17 \pm 6$
R21 $\chi^2$	$-5.878 \pm 0.027$	$-3.313 \pm 0.032$	$-0.10 \pm 0.11$	$-11 \pm 6$
<b>C27 + LMC + N4258</b>				
Disk prior, selection modelling	$-5.916 \pm 0.024$	$-3.335 \pm 0.033$	$-0.15 \pm 0.09$	$2 \pm 9$
Disk prior, no selection	$-5.924 \pm 0.024$	$-3.336 \pm 0.033$	$-0.18 \pm 0.09$	$-4 \pm 9$
R21 $\chi^2$	$-5.912 \pm 0.024$	$-3.328 \pm 0.033$	$-0.13 \pm 0.09$	$2 \pm 9$

**Table B1.** Posterior means and standard deviations for the C22 and C27 campaigns analysed separately, each combined with the LMC and N4258. Layout follows Table 4. The C22 selection does not include the extinction cut  $A_H < 0.4$  mag; the effect of including it is discussed in Section 5.4.

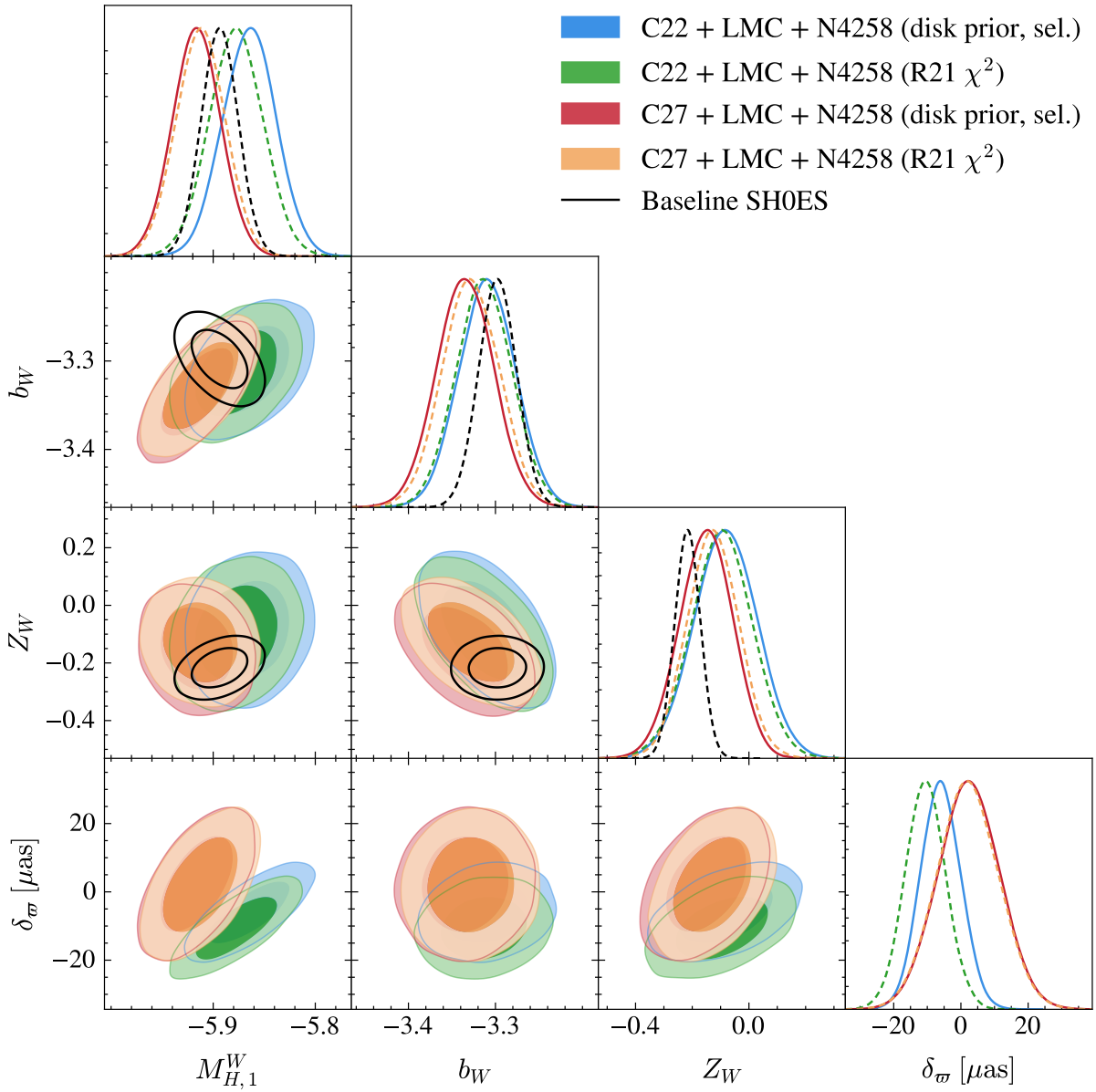


**Figure B1.** Marginalised posteriors of  $(M_{H,1}^W, b_W, Z_W, \delta_\varpi)$  for the individual C22+LMC+N4258 (blue, filled) and C27+LMC+N4258 (red, filled) configurations with disk prior and selection modelling. The corresponding R21  $\chi^2$  contours are shown for C22 (green, filled) and C27 (orange, filled), and the baseline SH0ES contours from R22 in black. All contours show the  $1\sigma$  and  $2\sigma$  credible regions.

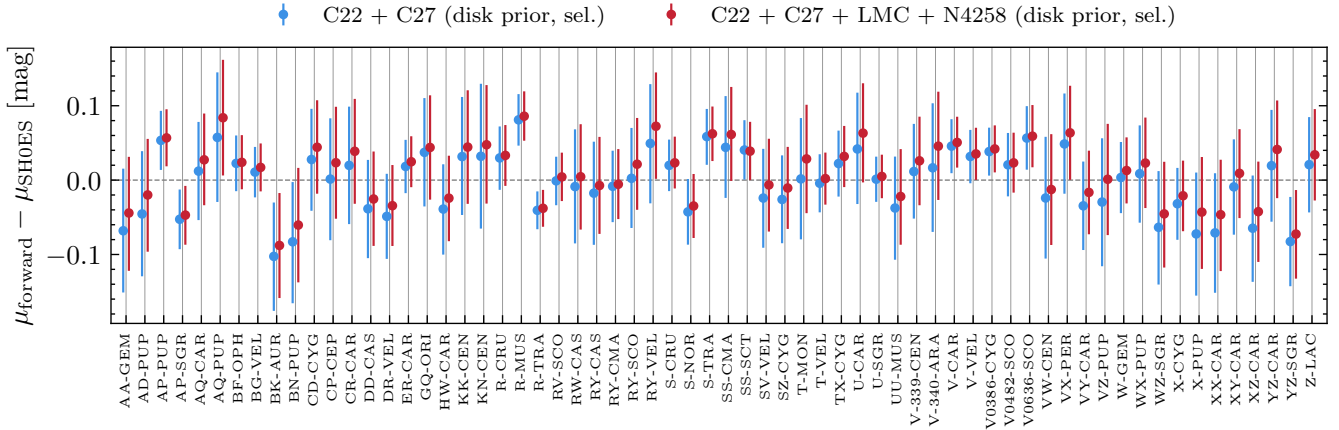


**Figure C1.** Per-star distance modulus residuals  $\langle \mu_{\text{forward}} \rangle - \mu_{\text{SH0ES}}$  for each MW Cepheid, comparing the MW-only model (blue) and the fiducial model including the LMC and N4258 (red). The reference  $\mu_{\text{SH0ES}}$  is computed from the observed Wesenheit magnitude and the baseline SH0ES period–luminosity parameters. Error bars span the 16th–84th percentiles of the posterior. Stars are sorted alphabetically by name; vertical grid lines indicate individual Cepheids.

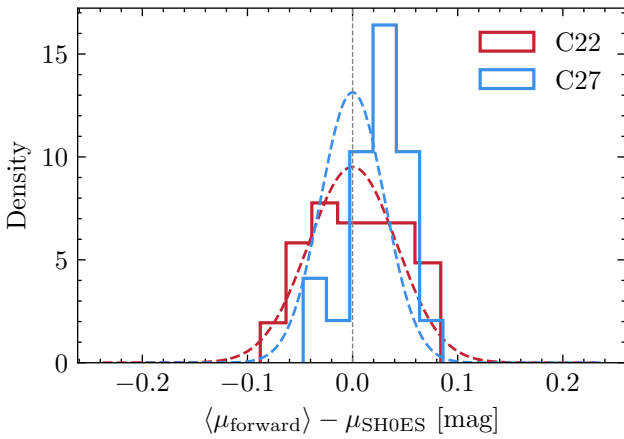


**Figure C2.** Distribution of per-star posterior-mean distance modulus residuals  $\langle \mu_{\text{forward}} \rangle - \mu_{\text{SH0ES}}$  for C22 (red) and C27 (blue) from the fiducial model. Dashed lines show zero-mean Gaussians with standard deviations matched to each campaign.

### D1 Parallax selection

For a parallax selection  $\mathcal{S}(\varpi_{\text{obs}}) = \Theta(\varpi_{\text{obs}} - \varpi_{\text{min}})$ , modelled as a step function, integrating the parallax likelihood against the selection gives

$$\int_{\varpi_{\text{min}}}^{\infty} d\varpi_{\text{obs}} \mathcal{N}(\varpi_{\text{obs}} | v - \delta_{\varpi}, \sigma_{\varpi}^2) = \Phi\left(\frac{v - \delta_{\varpi} - \varpi_{\text{min}}}{\sigma_{\varpi}}\right), \quad (\text{D14})$$

where  $v = 1/d$  is the geometric parallax. Since  $\mathcal{S}$  depends only on  $\varpi_{\text{obs}}$ , the magnitude likelihood integrates to unity over  $m_{H,\text{obs}}^W$  for any  $\sigma_1$ . Marginalising over the distance with the uniform-in-volume prior ( $v^{-4} = d^2 |dd/dv|$ ), the detection probability is

$$p(S = 1 | \delta_{\varpi}) \propto \int dv v^{-4} \Phi\left(\frac{v - \delta_{\varpi} - \varpi_{\text{min}}}{\sigma_{\varpi}}\right). \quad (\text{D15})$$

The detection probability is independent of the period–luminosity relation parameters ( $M_{H,1}^W$ ,  $b_W$ ,  $Z_W$ ), since  $M$  has dropped out entirely. To evaluate the integral analyt-

ically, we take the sharp-cut limit  $\sigma_{\varpi} \rightarrow 0$ , in which the parallax measurement errors are assumed to have a negligible effect on the selection. Then  $\Phi \rightarrow \Theta(v - \delta_{\varpi} - \varpi_{\text{min}})$  and the integral evaluates to

$$p(S = 1 | \delta_{\varpi}) \propto \int_{\varpi_{\text{min}} + \delta_{\varpi}}^{\infty} dv v^{-4} = \frac{1}{3} (\varpi_{\text{min}} + \delta_{\varpi})^{-3}. \quad (\text{D16})$$

Applying this approximation to the detection probability while retaining the full parallax uncertainty in the marginal likelihood, the selection-adjusted likelihood is

$$\frac{\mathcal{L}^{\text{marg}}}{p(S = 1 | \delta_{\varpi})} \propto \left(\frac{\varpi_{\text{min}} + \delta_{\varpi}}{\varpi_{\text{phot}}}\right)^3 \mathcal{N}(\varpi_{\text{obs}} | \varpi_{\text{phot}} - \delta_{\varpi}, \tilde{\sigma}_{\varpi}^2). \quad (\text{D17})$$

### D2 Magnitude selection

We now consider a selection on the Wesenheit magnitude,  $\mathcal{S}(m) = \Theta(m_{H,\text{max}}^W - m_{H,\text{obs}}^W)$ , imposing a faint-end limit. As before, because  $\mathcal{S}$  depends on  $m_{H,\text{obs}}^W$  rather than  $\varpi_{\text{obs}}$ , the parallax likelihood integrates to unity over  $\varpi_{\text{obs}}$ . Integrating the magnitude likelihood against the selection,

$$\int_{-\infty}^{m_{H,\text{max}}^W} dm \mathcal{N}(m | M + \mu(d), \sigma_1^2) = \Phi\left(\frac{m_{H,\text{max}}^W - M - \mu(d)}{\sigma_1}\right), \quad (\text{D18})$$

so the marginalised detection probability becomes

$$p(S = 1 | \theta) \propto \int_0^{\infty} dd d^2 \Phi\left(\frac{m_{H,\text{max}}^W - M - \mu(d)}{\sigma_1}\right), \quad (\text{D19})$$

which, unlike the parallax selection of Eq. (D15), depends on the period–luminosity relation parameters through  $M$  (but not  $\delta_{\varpi}$ ). In a similar sharp-cut limit ( $\sigma_1 \rightarrow 0$ ), the step function imposes an upper distance cut at  $d_{\text{max}}$  defined by  $\mu(d_{\text{max}}) = m_{H,\text{max}}^W - M$ , corresponding to

$$\varpi_{\text{min}}^{(m)} \equiv 1/d_{\text{max}} = 10^{-0.2(m_{H,\text{max}}^W - M - 10)}. \quad (\text{D20})$$

The integral then evaluates to

$$p(S = 1 | \theta) \propto d_{\text{max}}^3 = \left(\varpi_{\text{min}}^{(m)}\right)^{-3}. \quad (\text{D21})$$

The parallax ratio entering the selection-adjusted likelihood is

$$\frac{\varpi_{\min}^{(m)}}{\varpi_{\text{phot}}} = \frac{10^{-0.2(m_{H,\text{max}}^W - M - 10)}}{10^{-0.2(m_{H,\text{obs}}^W - M - 10)}} \quad (\text{D22})$$

$$= 10^{-0.2(m_{H,\text{max}}^W - m_{H,\text{obs}}^W)},$$

which is a per-star constant independent of  $\theta$ . The selection-adjusted marginal likelihood under a magnitude cut therefore reduces to

$$\frac{\mathcal{L}^{\text{marg}}}{p(S=1|\theta)} \propto \mathcal{N}(\varpi_{\text{obs}} | \varpi_{\text{phot}} - \delta_{\varpi}, \tilde{\sigma}_{\varpi}^2). \quad (\text{D23})$$

### D3 Summary

The results above rest on two approximations: the linearisation of  $\mu(\varpi)$ , which is accurate when the intrinsic magnitude scatter  $\sigma_1$  is small, and the sharp-cut evaluation of the detection probabilities, which assumes that observational errors have a negligible effect on the selection. Had we instead adopted  $\pi(d) \propto d^k$  for arbitrary  $k$ , the prefactor and detection probability would both scale as the  $(k+1)$ -th power of the geometric parallax: the magnitude-selection cancellation would remain exact, and the parallax-selection ratio would retain the same structure with exponent  $k+1$  in place of 3. The Galactic thin-disk prior used in the main text is not a simple power law, so the magnitude-selection cancellation is no longer exact; the ratio  $\varpi_{\min}^{(m)}/\varpi_{\text{phot}}$  remains a per-star constant, but the prior-dependent prefactor no longer reduces to a simple power of this ratio. We verify in the main text that the choice of distance prior has a negligible effect on the inferred parameters once the selection is self-consistently accounted for in the forward model, because the per-star likelihood localises each distance to a narrow range over which the disk geometry varies minimally. In Appendix E we show on mock data that for both magnitude- and parallax-selected samples, the linearised Gaussian with selection and the  $\chi^2$  approach yield consistent results, with neither exhibiting significant bias in the inferred period–luminosity parameters.

For a magnitude-selected sample, the linearised Gaussian per-star likelihood differs from the  $\chi^2$  only by the prefactor

$$\frac{1}{\tilde{\sigma}_{\varpi}} = \frac{1}{\sqrt{\left(\frac{\ln 10}{5}\right)^2 \varpi_{\text{phot}}^2 \sigma_1^2 + \sigma_{\varpi}^2}}. \quad (\text{D24})$$

Because the parallax measurement uncertainty dominates the error budget, with the photometric contribution  $(\ln 10/5) \varpi_{\text{phot}} \sigma_1$  being small when the intrinsic scatter  $\sigma_1$  is small, we have  $\tilde{\sigma}_{\varpi} \approx \sigma_{\varpi}$ , a per-star constant independent of the model parameters  $\theta$ . The prefactor therefore drops out of the posterior and the two methods yield identical inferences.

For a parallax-selected sample, the linearised Gaussian carries an additional factor

$$\left(\frac{\varpi_{\min} + \delta_{\varpi}}{\varpi_{\text{phot}}}\right)^3 \frac{1}{\tilde{\sigma}_{\varpi}}. \quad (\text{D25})$$

The  $1/\tilde{\sigma}_{\varpi}$  term is again negligible for the same reason. The cubic ratio in principle depends on  $\theta$  through both  $\varpi_{\text{phot}}$  and  $\delta_{\varpi}$ ; however, since  $|\delta_{\varpi}| \sim 10 \mu\text{as}$  is much smaller

than the selection threshold  $\varpi_{\min} = 800 \mu\text{as}$ , the numerator  $\varpi_{\min} + \delta_{\varpi} \approx \varpi_{\min}$  is effectively constant with respect to  $\delta_{\varpi}$ . The ratio then reduces to  $(\varpi_{\min}/\varpi_{\text{phot}})^3$ , which still depends on  $\theta$  through  $\varpi_{\text{phot}}$ , but for most C27 stars the photometric parallax is close to the selection threshold ( $\varpi_{\text{phot}} \approx \varpi_{\min}$ ), driving this ratio towards unity. The entire correction factor is therefore approximately negligible. In Appendix E we verify these conclusions on mock data, additionally testing the full forward model derived in the main text and probing the effect of higher intrinsic scatter.

## APPENDIX E: VALIDATION ON MOCK DATA

We validate the inference framework on mock catalogues that mimic the C22 and C27 observational campaigns separately, isolating the effect of the magnitude-limited and parallax-limited selection functions.

For each mock realisation, we generate a parent population of Cepheids as follows. Per-star distances are drawn from a uniform-in-volume prior (adopted for simplicity in this mock example),

$$\pi(d) \propto d^2, \quad d \in [0.3, d_{\text{max}}] \text{ kpc}, \quad (\text{E1})$$

where  $d_{\text{max}} = 10$  kpc for the C22 mock and  $d_{\text{max}} = 2$  kpc for the C27 mock; in both cases  $d_{\text{max}}$  is much larger than the distances of any stars retained after selection, so the upper boundary does not affect the selected sample. The parent population sizes  $N_{\text{parent}} = 2000$  for C22 and  $N_{\text{parent}} = 100$  for C27 are chosen so that after selection the mock catalogues contain approximately 47 and 26 stars, respectively, comparable to the real samples. True pulsation periods and metallicities are drawn from Gaussian distributions,

$$\log P \leftarrow \mathcal{N}(\mu_{\log P}, \sigma_{\log P}^2),$$

$$[\text{O}/\text{H}] \leftarrow \mathcal{N}(0, 0.15^2), \quad (\text{E2})$$

with  $(\mu_{\log P}, \sigma_{\log P}) = (0.8, 0.3)$  for C22 and  $(0.75, 0.2)$  for C27. Given the sampled distances, periods, and metallicities, we compute absolute Wesenheit magnitudes from the period–luminosity relation (Eq. (8)) with fiducial parameters  $(M_{H,1}^W, b_W, Z_W) = (-5.90, -3.30, -0.22)$  and intrinsic scatter  $\sigma_{\text{int}} = 0.06$  mag. Observed magnitudes and parallaxes are then drawn from the per-star likelihoods,

$$m_{H,\text{obs}}^W \leftarrow \mathcal{N}\left(m_{H,\text{pred}}^W, \sigma_m^2 + \sigma_{\text{int}}^2\right),$$

$$\varpi_{\text{obs}} \leftarrow \mathcal{N}(1/d_i - \delta_{\varpi}, \sigma_{\varpi}^2), \quad (\text{E3})$$

with  $\sigma_m = 0.028$  mag,  $\sigma_{\varpi} = 0.019$  mas (matching the median uncertainties of the MW Cepheid catalogue), and fiducial offset  $\delta_{\varpi} = -0.014$  mas.

The selection function is then applied to the parent sample. For C22, we impose an upper apparent-magnitude limit  $m_{H,1}^W < 6.5$  mag and a lower period cut  $P > 8$  days. For C27, we impose a lower parallax cut with threshold  $\varpi_{\min} = 0.8$  mas and transition width  $w_{\varpi} = 0.05$  mas; we verify that selecting instead on the photometric parallax with period–luminosity parameters slightly offset from the true values yields no significant difference in the bias tests. We adopt wide uniform priors on all inferred parameters.

We compare three inference approaches applied to each mock: (i) the linearised Gaussian likelihood (Eq. (D12)), incorporating the magnitude-selection

factor for C22 (Eq. (D23)) and the parallax-selection factor for C27 (Eq. (D17)); (ii) the R21  $\chi^2$  method (Eq. (49)), which does not model selection explicitly; and (iii) the full forward model derived in the main text, which samples per-star distances from the disk prior and self-consistently accounts for selection. For each mock realisation and inference method, we record the normalised bias for each parameter  $\theta$ ,

$$b_\theta = \frac{\hat{\theta} - \theta_{\text{true}}}{\sigma_\theta}, \quad (\text{E4})$$

where  $\hat{\theta}$  and  $\sigma_\theta$  are the posterior mean and standard deviation. For an unbiased result with correct uncertainty calibration and approximately Gaussian posteriors away from prior boundaries,  $b_\theta$  follows a standard normal distribution across realisations; both conditions are satisfied here. We repeat the test at two values of the intrinsic scatter:  $\sigma_{\text{int}} = 0.06$  mag, consistent with the value inferred from the real data, and an artificially inflated  $\sigma_{\text{int}} = 0.15$  mag to probe the regime in which the approximations of Appendix D begin to break down.

Figure E1 shows the distribution of  $b_\theta$  for all inferred parameters over 10 000 mock realisations. At the fiducial scatter (Fig. E1a), all three methods recover the input parameters without significant bias for both C22 and C27, with the  $\chi^2$  method showing only a modest  $0.26\sigma$  bias in  $\delta_\varpi$  for C27, consistent with the parallax truncation effect derived in Section D1. The slope  $b_W$  is similarly unbiased across all configurations. The metallicity coefficient  $Z_W$  shows a  $\sim 0.3\sigma$  bias under both the  $\chi^2$  and linearised Gaussian methods, because neither accounts for the intrinsic scatter of the metallicity values; the forward model, which does, recovers  $Z_W$  without bias.

At the inflated scatter (Fig. E1b), the  $\chi^2$  method develops mild biases for C22:  $0.69\sigma$  in  $M_{H,1}^W$  and  $1.03\sigma$  in  $\delta_\varpi$ , while the linearised Gaussian shows a smaller  $0.43\sigma$  bias in  $M_{H,1}^W$ . The forward model remains well calibrated throughout. This demonstrates that, at the fiducial scatter of the real data, the approximations underlying the  $\chi^2$  and linearised Gaussian methods are reasonable, but would break down were the intrinsic scatter substantially larger.

This paper has been typeset from a  $\text{\TeX}/\text{\LaTeX}$  file prepared by the author.

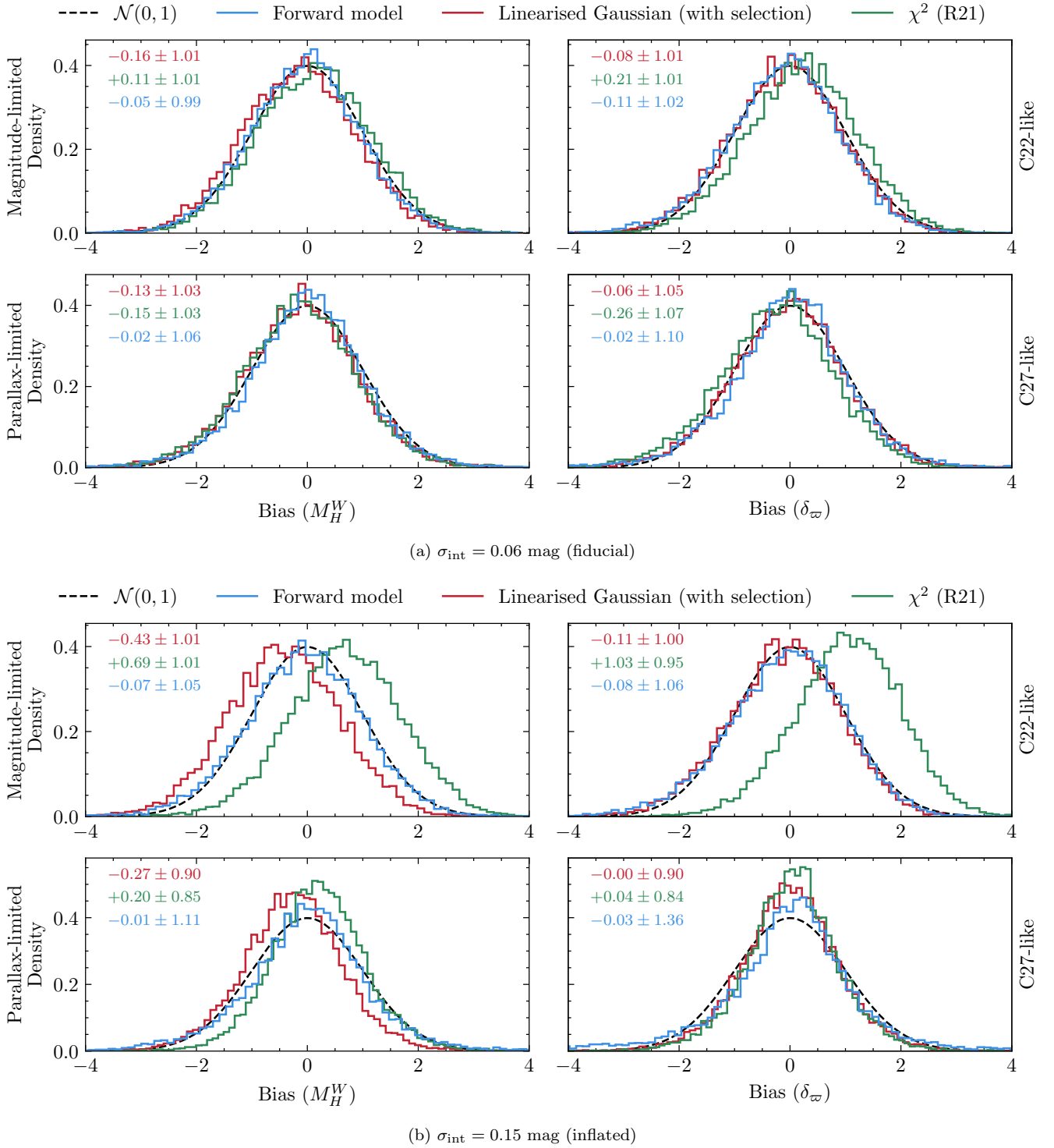


**Figure E1.** Normalised bias  $b_\theta = (\hat{\theta} - \theta_{\text{true}})/\sigma_\theta$  over 10 000 mock realisations of C22 (upper rows) and C27 (lower rows), for the linearised Gaussian (red), the R21  $\chi^2$  (green), and the forward model (blue). The dashed curve is  $\mathcal{N}(0, 1)$ . At the fiducial scatter (panel a), all three methods are approximately unbiased (Appendix D). At inflated scatter (panel b), the  $\chi^2$  method develops significant biases in  $M_{H,1}^W$  and  $\delta_\varpi$  for C22, while the other two remain well calibrated. Annotations give the mean and standard deviation of  $b_\theta$ .